

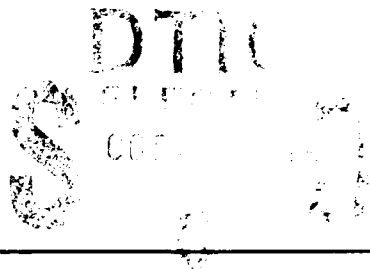
AD-A241 015



2

TECHNICAL REPORT BRL-TR-3265

BRL



TRANSONIC NAVIER-STOKES COMPUTATIONS
FOR A SPINNING BODY OF REVOLUTION

JUBARAJ SAHU

SEPTEMBER 1991

91-12151

APPROVED FOR PUBLIC RELEASE; DISTRIBUTION IS UNLIMITED.

U.S. ARMY LABORATORY COMMAND

BALLISTIC RESEARCH LABORATORY
ABERDEEN PROVING GROUND, MARYLAND

NOTICES

Destroy this report when it is no longer needed. DO NOT return it to the originator.

Additional copies of this report may be obtained from the National Technical Information Service, U.S. Department of Commerce, 5285 Port Royal Road, Springfield, VA 22161.

The findings of this report are not to be construed as an official Department of the Army position, unless so designated by other authorized documents.

The use of trade names or manufacturers' names in this report does not constitute endorsement of any commercial product.

UNCLASSIFIED

REPORT DOCUMENTATION PAGE			Form Approved OMB No. 0704-0188	
Public reporting burden for this collection of information is estimated to average 1 hour per response, including the time for reviewing instructions, searching existing data sources, gathering and maintaining the data needed, and completing and reviewing the collection of information. Send comments regarding this burden estimate or any other aspect of this collection of information, including suggestions for reducing this burden, to Washington Headquarters Services, Directorate for Information Operations and Reports, 1215 Jefferson Davis Highway, Suite 1204, Arlington, VA 22202-4302, and to the Office of Management and Budget, Paperwork Reduction Project (0704-0188), Washington, DC 20503.				
1. AGENCY USE ONLY (Leave blank)		2. REPORT DATE September 1991		3. REPORT TYPE AND DATES COVERED Final, July 1989 - July 1991
4. TITLE AND SUBTITLE TRANSONIC NAVIER-STOKES COMPUTATIONS FOR A SPINNING BODY OF REVOLUTION			5. FUNDING NUMBERS 1L161102AH43 61102A-00-001 AJ	
6. AUTHOR(S) JUBARAJ SAHU			8. PERFORMING ORGANIZATION REPORT NUMBER	
7. PERFORMING ORGANIZATION NAME(S) AND ADDRESS(ES)				
9. SPONSORING/MONITORING AGENCY NAME(S) AND ADDRESS(ES) US Army Ballistic Research Laboratory ATTN: SLCBR-DD-T Aberdeen Proving Ground, Maryland 21005-5066			10. SPONSORING/MONITORING AGENCY REPORT NUMBER BRL-TR-3265	
11. SUPPLEMENTARY NOTES				
12a. DISTRIBUTION/AVAILABILITY STATEMENT Approved for public release; distribution is unlimited.			12b. DISTRIBUTION CODE	
13. ABSTRACT (Maximum 200 words) A zonal, implicit, time-marching Navier-Stokes computational technique has been used to compute three dimensional transonic flow fields over a projectile. Flow field computations have been performed at M = 0.94 for spin rates of 0 and 4900 rpm and at angles of attack, alpha = 0, 4, and 10 degrees. All the computations have been performed on the Cray-2 supercomputer. Details of the flow field such as Mach number contours and surface pressure distributions are presented. Computed surface pressures are compared with available experimental data for the same conditions and the same configuration. Computed results show the large circumferential pressure distribution over the boattail region as well as the nonlinear effect of the angle of attack. Aerodynamic force and moment coefficients (normal force, pitching moment, Magnus force, and Magnus moment) have been obtained from the computed pressures and are compared with the data. The computed results are generally in good agreement with the data at low angle of attack for both nonspinning and spinning conditions. At high angle of attack the agreement is good for the nonspinning case and is less satisfactory for the spinning case.				
14. SUBJECT TERMS Aerodynamics Three Dimensional Flow Spinning Transonic Flow			15. NUMBER OF PAGES 37	
			16. PRICE CODE	
17. SECURITY CLASSIFICATION OF REPORT UNCLASSIFIED		18. SECURITY CLASSIFICATION OF THIS PAGE UNCLASSIFIED		19. SECURITY CLASSIFICATION OF ABSTRACT UNCLASSIFIED
			20. LIMITATION OF ABSTRACT UL	

INTENTIONALLY LEFT BLANK.

TABLE OF CONTENTS

	<u>Page</u>
LIST OF FIGURES	v
LIST OF TABLES	vi
1. INTRODUCTION	1
2. GOVERNING EQUATIONS AND SOLUTION TECHNIQUE	2
2.1 Governing Equations	2
2.2 Numerical Technique	4
2.3 Composite Grid Scheme	5
3. MODEL GEOMETRY AND EXPERIMENT	6
4. COMPUTATIONAL GRID AND COMPUTER RESOURCE	7
5. RESULTS	8
6. CONCLUDING REMARKS	27
7. REFERENCES	29
LIST OF SYMBOLS	31
DISTRIBUTION LIST	33



Accession For	
DTIC GRA&I	<input checked="" type="checkbox"/>
DTIC TAB	<input type="checkbox"/>
Unannounced	<input type="checkbox"/>
Justification	
By	
Distribution/	
Availability Codes	
Avail and/or	
Dist	Special
A-1	

INTENTIONALLY LEFT BLANK.

LIST OF FIGURES

<u>Figure</u>		<u>Page</u>
1	Model geometry	6
2	Computational grid (wind and lee side)	8
3	Expanded view of the base region grid	9
4	Mach number contours, $M_\infty=0.94$, $\alpha = 0.0^\circ$	10
5	Mach number contours, $M_\infty=0.94$, $\alpha = 4.0^\circ$	11
6	Mach number contours, $M_\infty=0.94$, $\alpha = 10.0^\circ$	11
7	Longitudinal surface pressure distribution, $M_\infty=0.94$, $\alpha = 0.0^\circ$	12
8	Longitudinal surface pressure distribution, $M_\infty=0.94$, $\alpha = 4.0^\circ$	12
9	Longitudinal surface pressure distribution, $M_\infty=0.94$, $\alpha = 10.0^\circ$	13
10	Circumferential surface pressure distribution, $P = 0$, $M_\infty=0.94$, $X/D=4.76$.	14
11	Circumferential surface pressure distribution, $P = 0$, $M_\infty=0.94$, $X/D=5.11$.	14
12	Circumferential surface pressure distribution, $P = 0$, $M_\infty=0.94$, $X/D=5.30$.	15
13	Circumferential surface pressure distribution, $P = 0$, $M_\infty=0.94$, $X/D=5.43$.	15
14	Circumferential surface pressure distribution, $P = 0$, $M_\infty=0.94$, $X/D=5.50$.	16
15	Circumferential surface pressure distribution, $P = 4900$ rpm, $M_\infty=0.94$, $X/D=4.76$	17
16	Circumferential surface pressure distribution, $P = 4900$ rpm, $M_\infty=0.94$, $X/D=5.11$	17
17	Circumferential surface pressure distribution, $P = 4900$ rpm, $M_\infty=0.94$, $X/D=5.30$	18
18	Circumferential surface pressure distribution, $P = 4900$ rpm, $M_\infty=0.94$, $X/D=5.43$	18
19	Circumferential surface pressure distribution, $P = 4900$ rpm, $M_\infty=0.94$, $X/D=5.50$	19
20	Circumferential surface pressure distribution, $M_\infty=0.94$, $\alpha = 4.0^\circ$, $X/D=4.76$	20
21	Circumferential surface pressure distribution, $M_\infty=0.94$, $\alpha = 10.0^\circ$, $X/D=4.76$	20
22	Circumferential surface pressure distribution, $M_\infty=0.94$, $\alpha = 4.0^\circ$, $X/D=5.43$	21
23	Circumferential surface pressure distribution, $M_\infty=0.94$, $\alpha = 10.0^\circ$, $X/D=5.43$	21
24	Normal force coefficient vs. angle of attack, $M_\infty=0.94$	22

25	Pitching moment coefficient vs. angle of attack, $M_\infty=0.94$	23
26	Development of Magnus force along the projectile, $M_\infty=0.94$	24
27	Magnus moment coefficient, $M_\infty=0.94$	25
28	Circumferential surface pressure distribution, $M_\infty=0.94$, $\alpha = 10.0^\circ$, $X/D=4.76$	26
29	Circumferential surface pressure distribution, $M_\infty=0.94$, $\alpha = 10.0^\circ$, $X/D=5.50$	27

LIST OF TABLES

<u>Table</u>		<u>Page</u>
1	Analysis of Nonlinear Magnus moment	25

1. INTRODUCTION

A spinning projectile in flight at angle of attack produces the Magnus effect. Many Army projectiles are slender, spin-stabilized bodies of revolution and at angle of attack are thus, subject to Magnus forces and moments. These forces and moments are generated by the distortion or asymmetry of the boundary layer with respect to the plane of angle of attack. Although the Magnus force is only a 10th to a 100th of the normal force, it is a critical parameter in determining the dynamic stability of shell. In addition, the critical aerodynamic behavior occurs in the transonic speed regime, $0.9 < M < 1.1$, where the aerodynamic coefficients have been found to increase by as much as 100 %. This flight regime is both experimentally and computationally difficult. Thus, only a limited number of experimental and computational studies have been made for spinning projectiles in this speed regime.

Numerical capabilities based on Navier-Stokes computational technique have been developed and used to compute three dimensional transonic flowfields (Nietubicz, Sturek, and Heavey 1983; Sahu 1987, 1988; Sahu and Steger 1987; Sahu and Nietubicz 1989). Earlier three dimensional computations for spinning (Nietubicz, Sturek, and Heavey 1983) and non-spinning (Sahu 1987) projectiles at transonic speed suffered from inadequate grid resolution. Recently, improved three dimensional (3D) predictions (Sahu and Steger 1987; Sahu 1988; Sahu and Nietubicz 1989) for non-spinning projectiles have been obtained using the Cray-2 supercomputer and a more advanced upwind flux-split algorithm. The critical aerodynamic behavior in pitching moment coefficient was successfully predicted using a zonal (Sahu and Steger 1987), implicit, time-marching Navier-Stokes scheme. This zonal scheme preserves the base corner and allows better modeling of the base region flow. The present research is a further extension and application of this technique to a spinning projectile at angles of attack up to 10 degrees.

The basic configuration used in this study has a 3.0 caliber nose, 2.1 caliber cylinder and a 7° , 0.5 caliber boattail. The experimental model was sting mounted from the base. As mentioned out earlier, a simple composite grid scheme has been used for accurate modeling of the base corner. Numerical flowfield computations have been performed at $M = 0.94$ for spin rates of 0 and 4900 rpm and at angles of attack, $\alpha = 0, 4$, and 10° . All the computations have been performed on the Cray-2 supercomputer. Details of the flowfield such as Mach number contours and surface pressure distributions are presented. Computed surface pressures are compared with available experimental data for the same conditions and the same configuration. Computed results show the large change in the circumferential pressure distribution over the boattail region as well as the non-linear effect

of the angle of attack. Aerodynamic force and moment coefficients (normal force, pitching moment coefficient, Magnus force, and Magnus moment) have been obtained from the computed pressures and are compared with the data.

2. GOVERNING EQUATIONS AND SOLUTION TECHNIQUE

The complete set of time-dependent thin-layer Navier-Stokes equations is solved numerically to obtain a solution to this problem. The numerical technique used is an implicit finite difference scheme. Although time-dependent calculations are made, the transient flow is not of primary interest at the present time. The steady flow, which is the desired result, is obtained in a time asymptotic fashion.

2.1 Governing Equations. The complete set of three dimensional, time dependent, generalized geometry, thin-layer, Navier-Stokes equations for general spatial coordinates ξ, η, ζ can be written as (Pulliam and Steger 1982):

$$\partial_\tau \hat{q} + \partial_\xi \hat{F} + \partial_\eta \hat{G} + \partial_\zeta \hat{H} = Re^{-1} \partial_\zeta \hat{S} \quad (1)$$

where

$$\begin{aligned} \xi &= \xi(x, y, z, t) && \text{- longitudinal coordinate} \\ \eta &= \eta(x, y, z, t) && \text{- circumferential coordinate} \\ \zeta &= \zeta(x, y, z, t) && \text{- nearly normal coordinate} \\ \tau &= t && \text{- time} \end{aligned}$$

and

$$\begin{aligned} \hat{q} &= \frac{1}{J} \begin{bmatrix} \rho \\ \rho u \\ \rho v \\ \rho w \\ e \end{bmatrix} & \hat{F} &= \frac{1}{J} \begin{bmatrix} \rho U \\ \rho u U + \xi_x p \\ \rho v U + \xi_y p \\ \rho w U + \xi_z p \\ (e + p)U - \xi_t p \end{bmatrix} \\ \hat{G} &= \frac{1}{J} \begin{bmatrix} \rho V \\ \rho u V + \eta_x p \\ \rho v V + \eta_y p \\ \rho w V + \eta_z p \\ (e + p)V - \eta_t p \end{bmatrix} & \hat{H} &= \frac{1}{J} \begin{bmatrix} \rho W \\ \rho u W + \zeta_x p \\ \rho v W + \zeta_y p \\ \rho w W + \zeta_z p \\ (e + p)W - \zeta_t p \end{bmatrix} \end{aligned} \quad (2)$$

and where

$$\hat{S} = \frac{1}{J} \begin{bmatrix} 0 \\ \mu(\zeta_x^2 + \zeta_y^2 + \zeta_z^2)u_\zeta + \frac{\mu}{3}(\zeta_x u_\zeta + \zeta_y v_\zeta + \zeta_z w_\zeta)\zeta_x \\ \mu(\zeta_x^2 + \zeta_y^2 + \zeta_z^2)v_\zeta + \frac{\mu}{3}(\zeta_x u_\zeta + \zeta_y v_\zeta + \zeta_z w_\zeta)\zeta_y \\ \mu(\zeta_x^2 + \zeta_y^2 + \zeta_z^2)w_\zeta + \frac{\mu}{3}(\zeta_x u_\zeta + \zeta_y v_\zeta + \zeta_z w_\zeta)\zeta_z \\ \{(\zeta_x^2 + \zeta_y^2 + \zeta_z^2)[\frac{\mu}{2}(u^2 + v^2 + w^2)_\zeta \\ + \frac{\kappa a_\zeta^2}{Pr(\gamma - 1)}] \\ + \frac{\mu}{3}(\zeta_x u + \zeta_y v + \zeta_z w)(\zeta_x u_\zeta + \zeta_y v_\zeta + \zeta_z w_\zeta)\} \end{bmatrix} \quad (3)$$

In equation (1), the thin-layer approximation is used and the viscous terms involving velocity gradients in both the longitudinal and circumferential directions are neglected. The viscous terms are retained in the normal direction, ζ , and are collected into the vector \hat{S} . These viscous terms are used everywhere except in the wake (or base region) where similar viscous terms are also added in the streamwise direction.

For this computation, the diffusion coefficients μ and κ contain molecular and turbulent parts. The turbulent contributions are supplied through an algebraic eddy-viscosity hypothesis which has been developed by Baldwin and Lomax (1978).

The velocities in the ξ , η , and ζ coordinate directions can be written

$$\begin{aligned} U &= \xi_t + u\xi_x + v\xi_y + w\xi_z \\ V &= \eta_t + u\eta_x + v\eta_y + w\eta_z \\ W &= \zeta_t + u\zeta_x + v\zeta_y + w\zeta_z \end{aligned}$$

which represent the contravariant velocity components.

The Cartesian velocity components (u , v , w) are retained as the dependent variables and are nondimensionalized with respect to a_∞ (the free stream speed of sound). The local pressure is determined using the relation

$$p = (\gamma - 1)[e - 0.5\rho(u^2 + v^2 + w^2)] \quad (4)$$

where γ is the ratio of specific heats. Density, ρ , is referenced to ρ_∞ and the total energy, e , to $\rho_\infty a_\infty^2$. The transport coefficients are also nondimensionalized with respect to the corresponding free stream variables. Thus the Prandtl number which appears in \hat{S} is defined as $Pr = c_{p\infty}\mu_\infty/\kappa_\infty$.

In differencing these equations it is often advantageous to difference about a known base solution denoted by subscript $_0$ as

$$\begin{aligned} \delta_\tau(\hat{Q} - \hat{Q}_0) + \delta_\xi(\hat{F} - \hat{F}_0) + \delta_\eta(\hat{G} - \hat{G}_0) + \delta_\zeta(\hat{H} - \hat{H}_0) - Re^{-1}\delta_\zeta(\hat{S} - \hat{S}_0) \\ = -\partial_\tau\hat{Q}_0 - \partial_\xi\hat{F}_0 - \partial_\eta\hat{G}_0 - \partial_\zeta\hat{H}_0 + Re^{-1}\partial_\zeta\hat{S}_0 \end{aligned} \quad (5)$$

where δ indicates a general difference operator, and ∂ is the differential operator. If the base state can be properly chosen, the differenced quantities can have smaller and smoother variation and therefore less of a differencing error (Pulliam and Steger 1982).

2.2 Numerical Technique. The implicit, approximately-factored, scheme for the thin layer Navier Stokes equations using central differencing in the η and ζ directions and upwinding in ξ is written in the following form

$$\begin{aligned} [I + h\delta_\xi^b(\hat{A}^+)^n + h\delta_\zeta\hat{C}^n - hRe^{-1}\bar{\delta}_\zeta J^{-1}\hat{M}^n J - D_i|_\zeta] \\ \times [I + h\delta_\xi^f(\hat{A}^-)^n + h\delta_\eta\hat{B}^n - D_i|_\eta] \Delta\hat{Q}^n = \\ -\Delta t\{\delta_\xi^b[(\hat{F}^+)^n - \hat{F}_\infty^+] + \delta_\xi^f[(\hat{F}^-)^n - \hat{F}_\infty^-] + \delta_\eta(\hat{G}^n - \hat{G}_\infty) \\ + \delta_\zeta(\hat{H}^n - \hat{H}_\infty) - Re^{-1}\bar{\delta}_\zeta(\hat{S}^n - \hat{S}_\infty)\} - D_e(\hat{Q}^n - \hat{Q}_\infty) \end{aligned} \quad (6)$$

where $h = \Delta t$ or $(\Delta t)/2$ and the free stream base solution is used. Here δ is typically a three point second order accurate central difference operator, $\bar{\delta}$ is a midpoint operator used with the viscous terms, and the operators δ_ξ^b and δ_ξ^f are backward and forward three-point difference operators. The flux \hat{F} has been eigensplit and the matrices \hat{A} , \hat{B} , \hat{C} , and \hat{M} result from local linearization of the fluxes about the previous time level. Here J denotes the Jacobian of the coordinate transformation. Dissipation operators, D_e and D_i are used in the central space differencing directions.

The smoothing terms used in the present study are of the form:

$$D_e|_\eta = (\Delta t)J^{-1}[\epsilon_2\bar{\delta}\rho(B)\beta\bar{\delta} + \epsilon_4\bar{\delta}\frac{\rho(B)}{1+\beta}\bar{\delta}^3]|_\eta J$$

$$D_i|_\eta = (\Delta t)J^{-1}[\epsilon_2\bar{\delta}\rho(B)\beta\bar{\delta} + 2.5\epsilon_4\bar{\delta}\rho(B)\bar{\delta}]|_\eta J$$

where $\beta = \frac{|\delta^2 p|}{|(1+\delta^2)p|}$ and where $\rho(B)$ is the true spectral radius of B . The idea here is that the fourth difference will be tuned down near shocks, that is, as β gets large the weight on the fourth difference drops down while the second difference tunes up.

For simplicity, most of the boundary conditions have been imposed explicitly (Sahu 1987). For the non-spinning cases, the wall temperature is specified on the body surface and the no-slip boundary condition is used at the wall. The pressure at the wall is calculated by solving a combined momentum equation. Free stream boundary conditions are used at the inflow boundary as well as at the outer boundary. A symmetry boundary condition is imposed at the circumferential edges of the grid while a simple extrapolation is used at the downstream boundary. A combination of symmetry and extrapolation boundary condition is used at the center line (axis). As mentioned in the introduction, the Magnus effect is produced by the spin induced distortion of the boundary layer. This requires the numerical calculations to be fully three dimensional since no plane of symmetry exists. For the spinning cases, spin or the non-dimensional angular velocity is provided through the contravariant, V term. In addition, a periodic implicit boundary condition is used in the circumferential direction. The flowfield is initially set to free stream conditions everywhere and then advanced in time until a steady state solution is obtained.

2.3 Composite Grid Scheme. In the present work, a simple composite grid scheme (Sahu 1988) has been used where a large single grid is split into a number of smaller grids so that computations can be performed on each of these grids separately. These grids use the available core memory one grid at a time, while the remaining grids are stored on an external disk storage device such as the solid state disk device (SSD) of the Cray X-MP/48 computer. The Cray-2 has a large incore memory to fit the large single grid. However, for accurate geometric modeling of complex projectile configurations which include blunt noses, sharp corners and base cavities, it is also desirable to split the large data base into a few smaller zones on the Cray-2 as well.

The use of a composite grid scheme requires special care in storing and fetching the interface boundary data, i.e., the communication between the various zones. In the present scheme, there is a one to one mapping of the grid points at the interface boundaries. Thus, no interpolations are required. Details of the data storage, data transfer and other pertinent information such as metric and differencing accuracy at the interfaces can be found in the work of Sahu and Steger (1988) and Sahu (1988). This scheme has been successfully

used by Sahu (1988) to compute three dimensional transonic flow over projectiles at angle of attack but without spin. The computed results clearly showed the transonic critical aerodynamic behavior of the pitching moment coefficient observed in free flight. The same technique was also applied to a more complicated projectile with base cavities (Sahu and Nietubicz 1989) and the wake flowfields were computed for these different configurations. The present work is a further application of this technique to the spinning projectile case.

3. MODEL GEOMETRY AND EXPERIMENT

The computational accuracy of a numerical scheme can be established through comparisons with available experimental data. The model used in the experiment and in the computational study is shown in Figure 1. It consists of a 3.0 caliber secant-ogive nose, a 2.0 caliber cylindrical section, and a 0.5 caliber 7° boattail. This configuration closely resembles the M549 155mm artillery shell. The model has a flat nose and is sting-mounted at the aft end of the projectile. Both of these are included in the numerical simulations for a direct comparison.

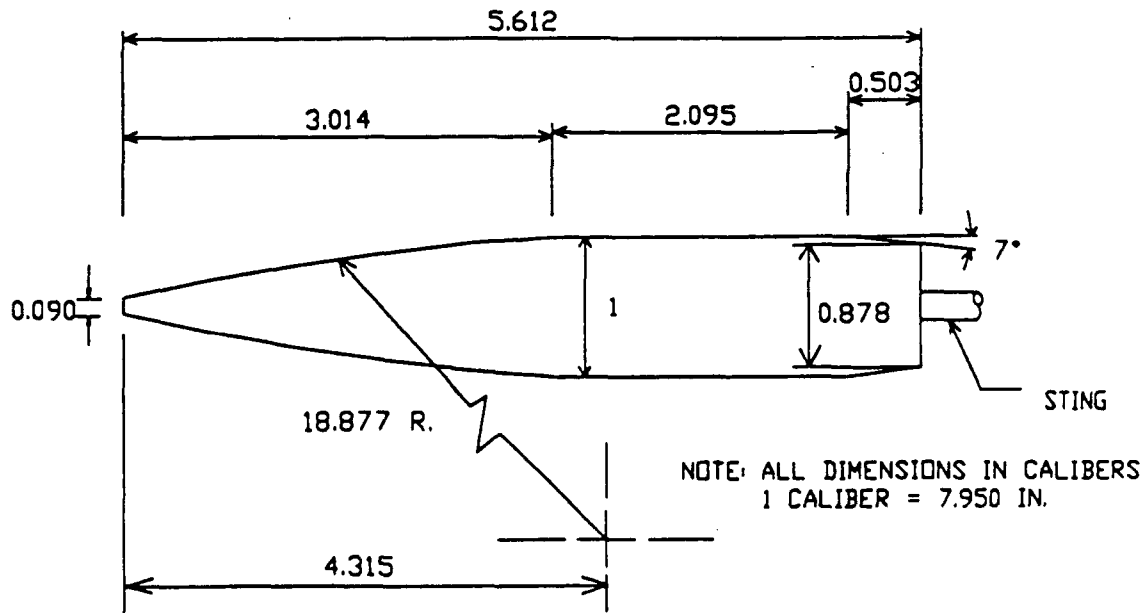


Figure 1. Model geometry.

Experimental measurements (Miller and Molnar 1986) for this model have been made at the NASA Ames 14 Foot Transonic Wind Tunnel. The model was tested at angles of attack of 0, 4, and 10 degrees and spin rates of 0 and 4900 rpm. Testing was conducted at a

Mach number of 0.94 and Reynolds number of 4×10^6 per foot. Circumferential pressures have been measured at several longitudinal positions on the model, with special emphasis on the cylindrical and boattail sections. These pressures have also been integrated to obtain the aerodynamic forces and moments which are available for comparison with the computed results.

4. COMPUTATIONAL GRID AND COMPUTER RESOURCE

The solution technique requires the discretization of the entire flow region of interest into a suitable computational grid. The grid outer boundary has been placed at 2.5 body lengths upstream and surrounding the projectile. The downstream boundary was placed at 2 body lengths. Since the calculations are in the subsonic/transonic regime the computational boundaries must extend out beyond the influence of the body. This ensures that the boundary conditions specified in the flow code are satisfied.

Since transonic flow fields are complex due to the presence of mixed subsonic and supersonic regions and shock waves, a large number of grid points are needed to capture the flow features. This is especially true of three dimensional transonic flows. Large computational grids require supercomputers with large memory and computing speeds.

Figure 2 shows a two-dimensional cross-section of the full 3D grid in the vicinity of the projectile. The surface points on the projectile as well as the longitudinal grid point distribution in the wake are selected using an interactive design program. The grid for the body region of the projectile was computed using a hyperbolic grid generation program (Nietubicz, Heavey, and Steger 1982). Each grid section was obtained separately and then appended to provide the full grid. The full grid is split into three zones, one in front of the nose, one on the projectile and the third one in the wake or base region. These grids consist of 30×79 , 175×50 and 59×99 grid points, respectively. The 3D grids consist of 39 points in the circumferential direction for the symmetric (non-spinning) case and 72 points for spinning case with no symmetry. An expanded view of the wake region grid is shown in Figure 3. It shows the longitudinal grid clustering on the boattail and near the base corner of the projectile. The grid points are also clustered near the projectile surface to capture the viscous effects in the boundary layer. For simplicity, this clustering has been extended from the base corner downstream into the wake region.

The current problem of interest is the effect of spin on the projectile aerodynamics. The large grids required for accurate numerical simulations of three dimensional transonic flows necessitates the use of a Cray class supercomputer. All numerical calculations for the

present study were made on the Cray-2 supercomputer at the Ballistic Research Laboratory (BRL). The numerical simulation of the non-spinning (symmetric) cases requires about 44 million words of central core memory on the Cray-2 whereas full 3D calculations for the spinning cases with no plane of symmetry requires about 82 million words of memory. Each of the numerical calculations for the symmetric case takes about 30 to 40 hours of computer time. The time required to get the final result for the spinning case is about two times that of the symmetric case.

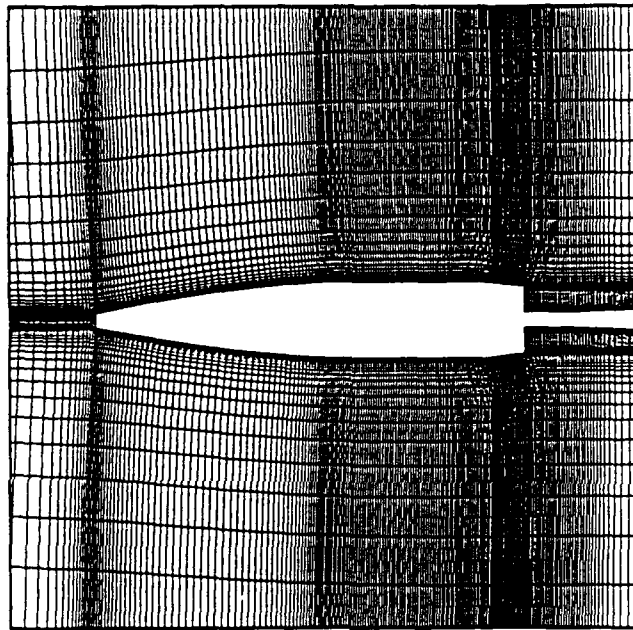


Figure 2. Computational grid (wind and lee side).

5. RESULTS

Numerical computations have been made for both spinning and non-spinning cases. All the computations have been run at $M_\infty = 0.94$ and $\alpha = 0, 4$ and 10° . Atmospheric flight conditions were used. The three plane version of the 3D code was run for the zero degree angle of attack case. For the non-spinning case, 39 planes were used in the circumferential direction. Two end planes were used to specify symmetric boundary conditions with the remaining 37 used for the circumferential half plane. The number of planes used for the full 3D spinning case was 72. For all these grids the circumferential grid spacing was 5° . For the zero angle of attack case, the grid was rotated circumferentially 5° on either side of the mid plane. This provided the 3 planes needed in the code to use central finite differences in the circumferential direction. In each case, the solution was marched from

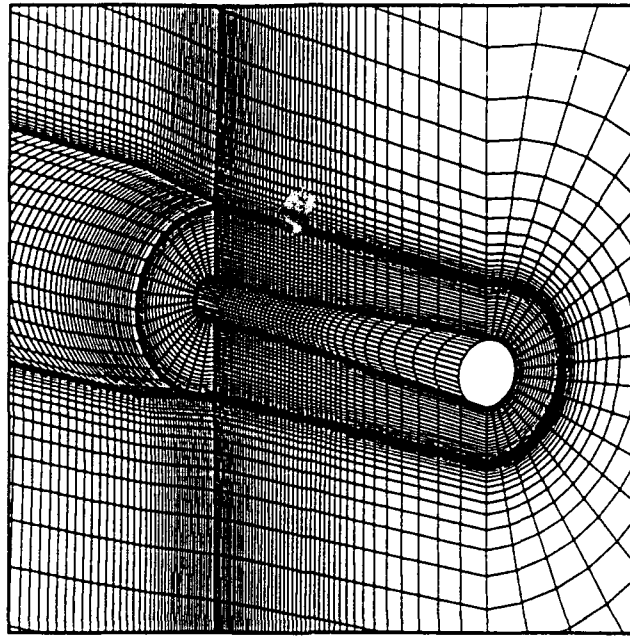


Figure 3. Expanded view of the base region grid.

free stream conditions everywhere until the final converged solution was obtained. The results are now presented in the form of surface pressure coefficients, and aerodynamic force and moment coefficients. Comparison of the computed results are made with the available experimental data (Miller and Molnar 1986). The computed force and moment coefficients are also compared with another set of experimental data (Platou and Nielsen 1973) where forces and moments were obtained using a force and moment balance.

A few qualitative results are presented next. Figures 4, 5, and 6 show typical Mach number contour plots for $M_\infty=0.94$ at $\alpha = 0, 4$, and 10° for the wind-side and the lee-side. Mixed regions of subsonic and supersonic flow have been determined. The subsonic regions are found in front of the flat nose, in the boundary layer and in the near wake. The flow regions near the ogive-cylinder junction as well as on the boattail are supersonic. Other features to observe are flow expansion at the ogive-cylinder and cylinder-boattail corners which are followed by shock waves (coalescence of contour lines) on the cylinder and boattail sections. For the zero degree angle of attack case (see Figure 4), the flow field was computed only for the top half plane and the flow field has been mirrored to emphasize the symmetric location of the shock waves along the body. As the angle of attack is increased to 4 degrees (Figure 5) the flow field becomes asymmetric. The shock waves are asymmetrically located (the wind-side shocks being closer to the base than the lee-side). This asymmetry is more pronounced with a further increase in angle of attack to 10 degrees. Figure 6 clearly shows the asymmetrically located shock waves for this case.

Figure 7 shows the longitudinal surface pressure distribution for the zero degree angle of attack case. Figure 8 and Figure 9 show the longitudinal surface pressure distribution for both the wind-side and lee-side at $\alpha = 4.0^\circ$ and $\alpha = 10.0^\circ$, respectively. In all these cases the computed surface pressures are found to be generally in good agreement with the experimental data (Miller and Molnar 1986). The flow expansions at the ogive and boattail corners are indicated by the pressure drop at these junctions. This is followed by a sharp increase in pressure at the shocks (on the cylinder and boattail). On the nose section of the projectile, for the angle of attack cases, the pressure on the wind-side ($\phi = 0.0^\circ$) is greater than the pressure acting on the lee-side ($\phi = 180.0^\circ$). The reverse is true on the boattail section. As shown in Figure 8 for $\alpha = 4.0^\circ$, the change in pressure between the wind-side and the lee-side on the cylindrical section is rather small. As angle of attack is increased to $\alpha = 10.0^\circ$, the difference in the wind-side and the lee-side pressures gets larger especially on the ogive and boattail sections (Figure 9).

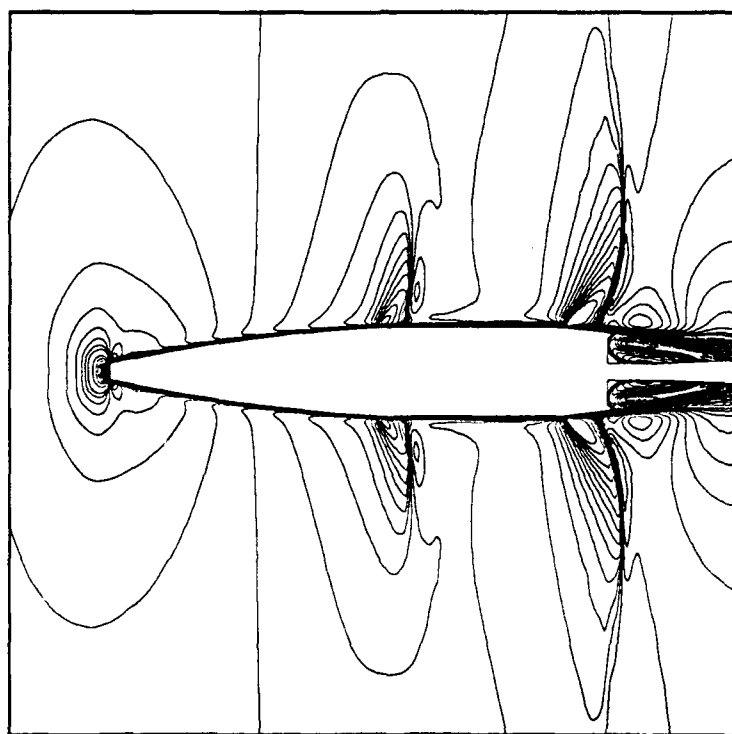


Figure 4. Mach number contours, $M_\infty=0.94$, $\alpha = 0.0^\circ$.

The next series of figures show the circumferential pressure distribution for both non-spinning and spinning cases. The results for the non-spinning cases are shown first. Here, $\phi = 0.0^\circ$ corresponds to the wind-side while the lee-side is at $\phi = 180.0^\circ$. Although, the computations are performed only for the half body, the computed circumferential pressure distributions have been mirrored and are shown for the full body i.e. for $\phi = 0$ to

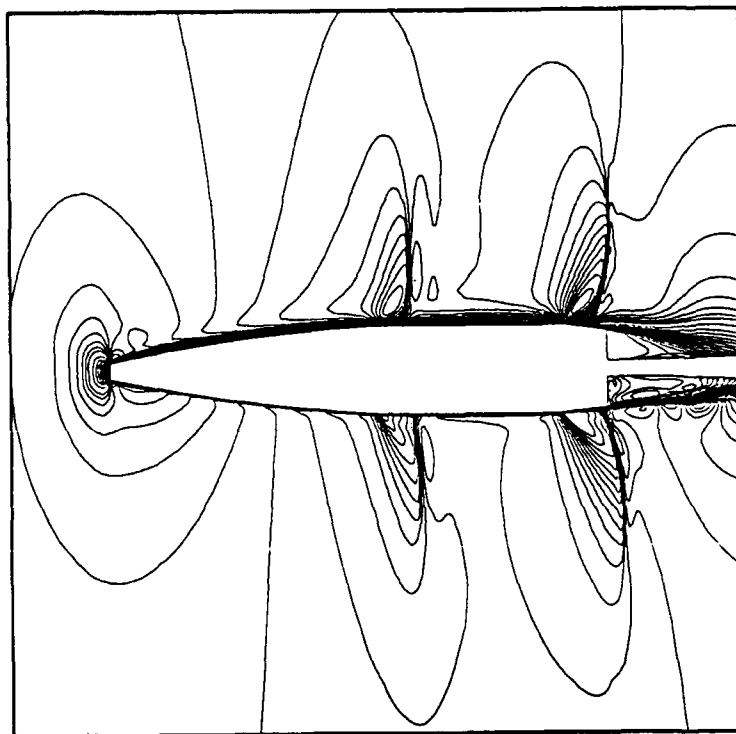


Figure 5. Mach number contours, $M_\infty=0.94$, $\alpha = 4.0^\circ$.

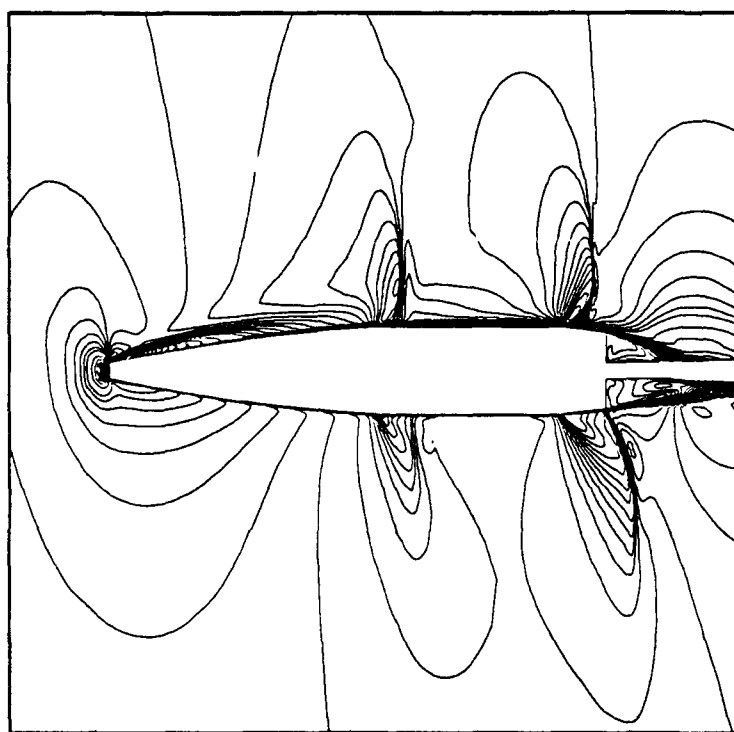


Figure 6. Mach number contours, $M_\infty=0.94$, $\alpha = 10.0^\circ$.

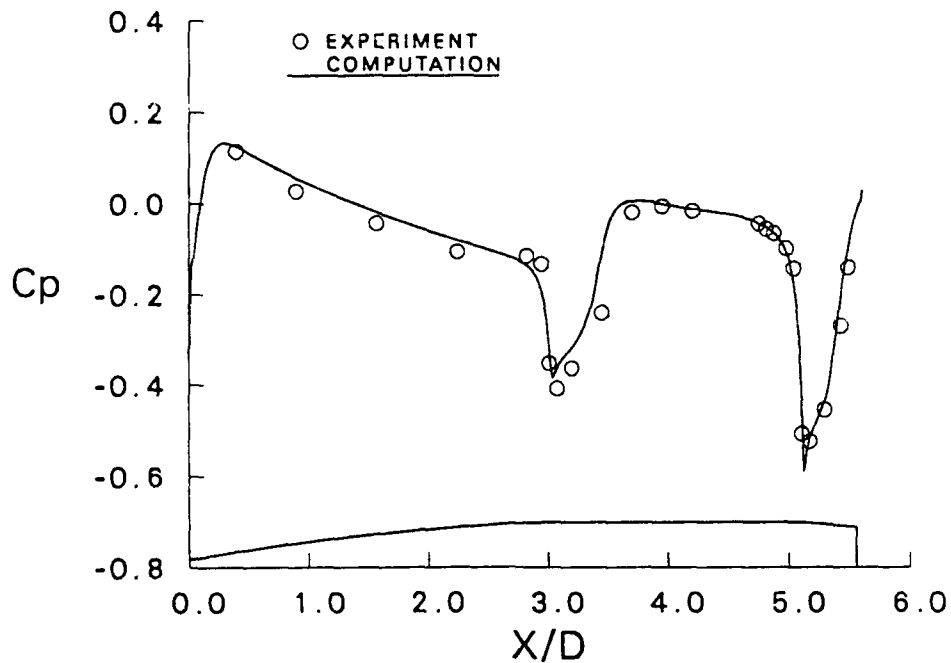


Figure 7. Longitudinal surface pressure distribution, $M_\infty=0.94$, $\alpha = 0.0^\circ$.

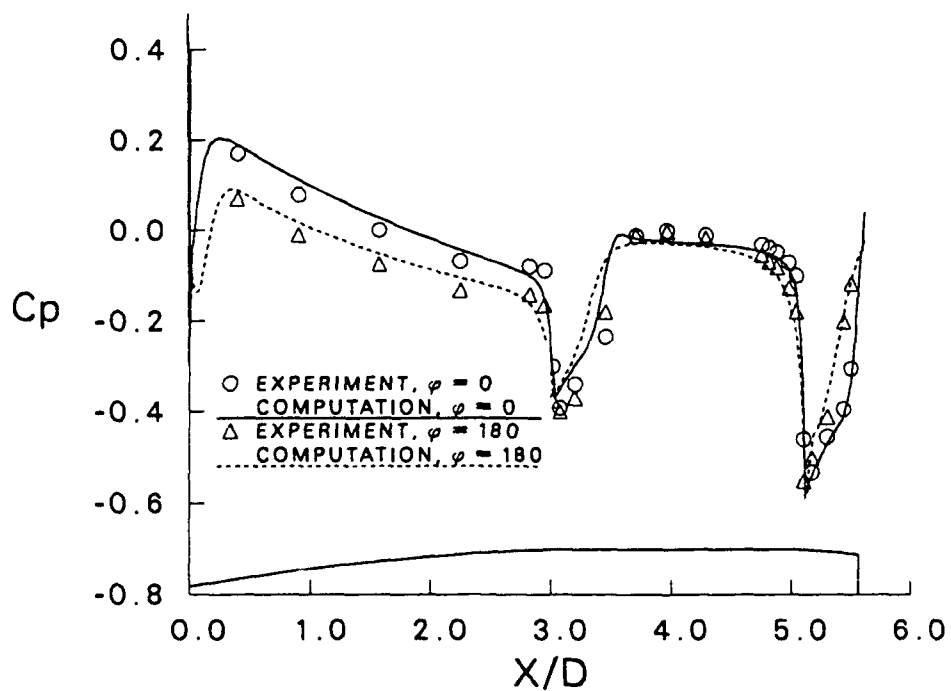


Figure 8. Longitudinal surface pressure distribution, $M_\infty=0.94$, $\alpha = 4.0^\circ$.

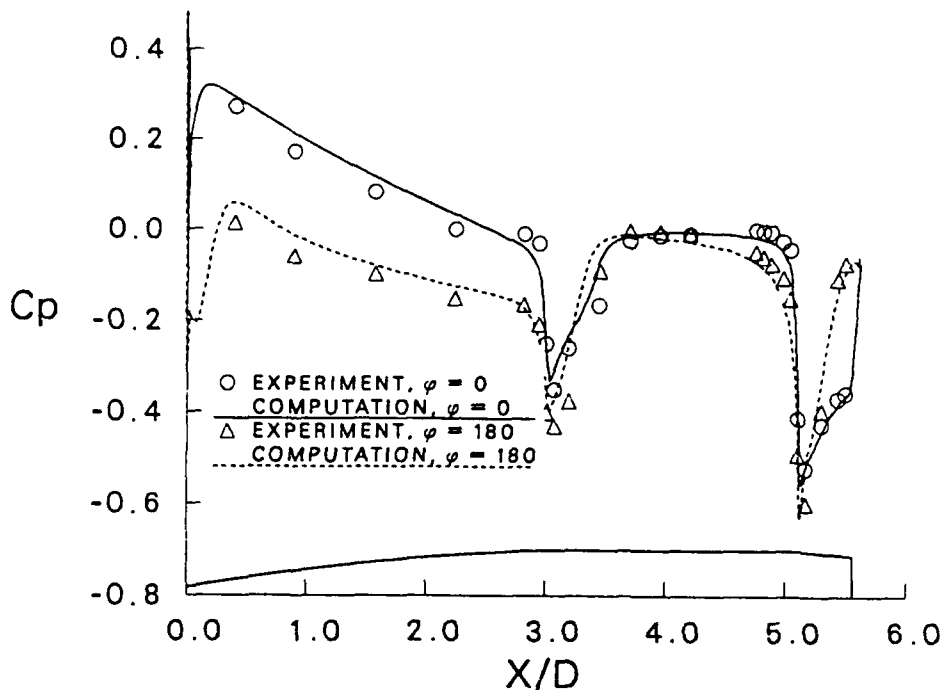


Figure 9. Longitudinal surface pressure distribution, $M_\infty=0.94$, $\alpha = 10.0^\circ$.

360.0°. Figure 10 shows the surface pressure distribution for a longitudinal position $X/D = 4.76$ which is on the cylindrical portion of the projectile ahead of the boattail corner. Figures 11 through 14 show the surface pressure distribution at $X/D = 5.11$, 5.30, 5.43, and 5.50, respectively. These longitudinal positions are all located on the boattail of the projectile. These figures show the effect of angle of attack on the pressure distribution. The computed pressures are compared with experimental data (Miller and Molnar 1986) in each of these figures. As seen in Figure 10 for $X/D = 4.76$, the variation of pressure with ϕ is almost negligible for $\alpha = 4.0^\circ$. However, at $\alpha = 10.0^\circ$ the pressure first drops and then increases in going from the wind-side to the lee-side. The computed pressures are in very good agreement with the data. For $X/D = 5.11$ (Figure 11), there exists a noticeable circumferential pressure variation for both $\alpha = 4.0^\circ$ and $\alpha = 10.0^\circ$. The extent of the circumferential variation in pressure increases with locations further aft on the boattail as shown in Figure 11 through Figure 14. For $\alpha = 4.0^\circ$, the pressure variation is small near the wind-side and then the pressure rises as the lee-side is approached. For $\alpha = 10.0^\circ$, however, the pressure first drops and then increases sharply as the lee-side is approached. Computed pressure peaks occur on the lee-side for both cases. The computed pressures are generally in good agreement with the experimental data. Also, as seen in these figures, large variations in surface pressures occur with increase in angle of attack.

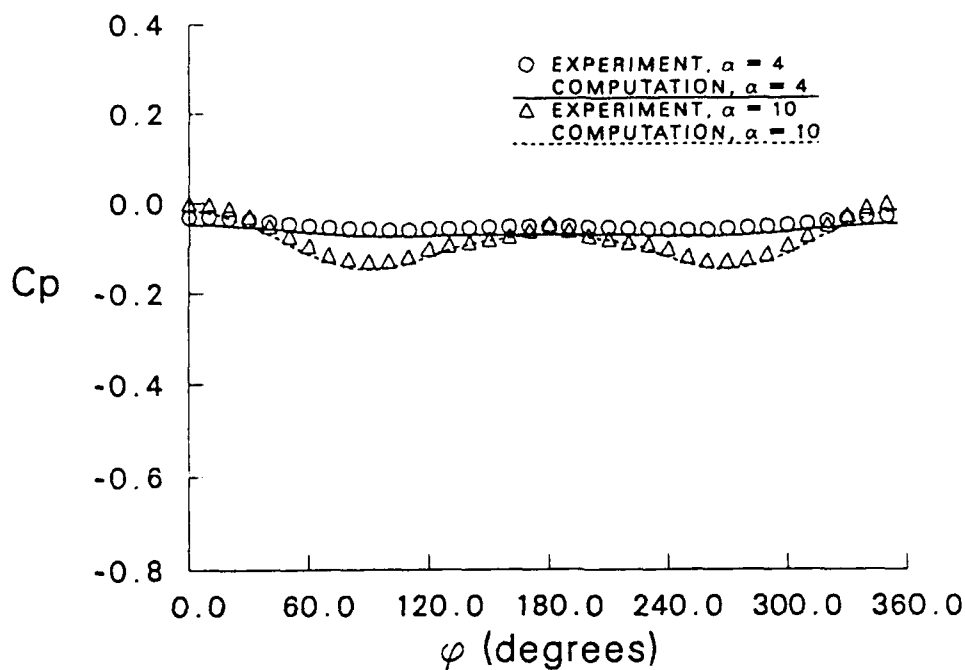


Figure 10. Circumferential surface pressure distribution, $P = 0$, $M_\infty = 0.94$, $X/D = 4.76$.

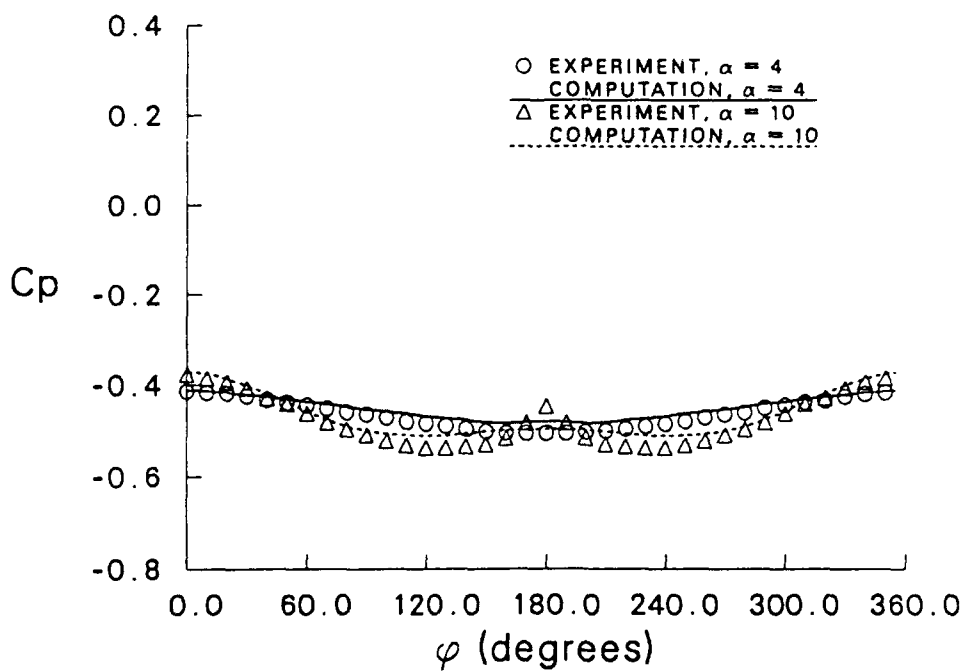


Figure 11. Circumferential surface pressure distribution, $P = 0$, $M_\infty = 0.94$, $X/D = 5.11$.

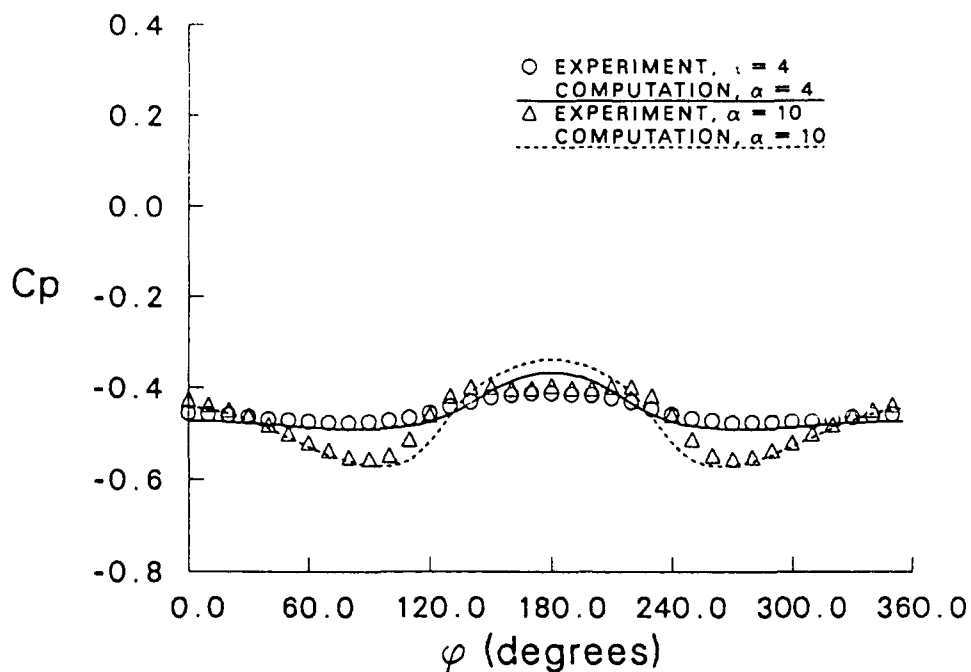


Figure 12. Circumferential surface pressure distribution, $P = 0$, $M_\infty = 0.94$, $X/D = 5.30$.

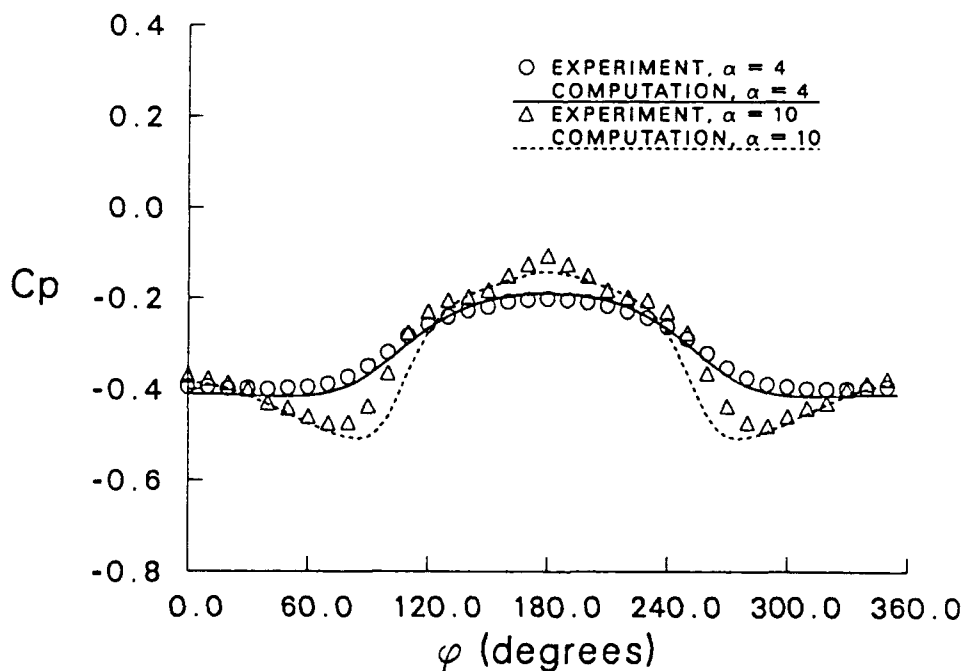


Figure 13. Circumferential surface pressure distribution, $P = 0$, $M_\infty = 0.94$, $X/D = 5.43$.

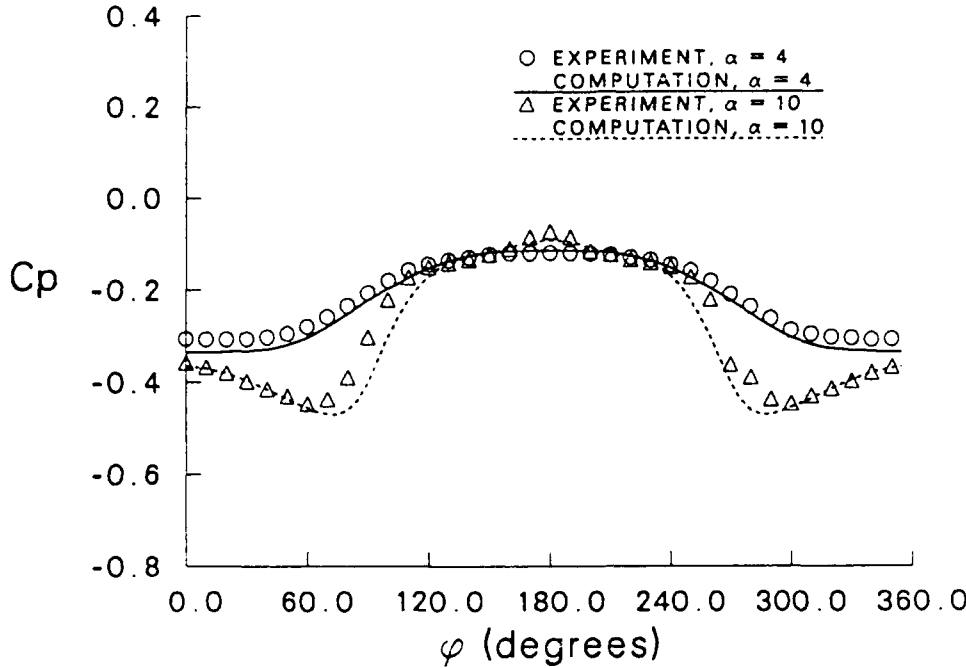


Figure 14. Circumferential surface pressure distribution, $P = 0$, $M_\infty = 0.94$, $X/D = 5.50$.

The results for the spinning cases are shown next. Here again the circumferential pressure distributions are shown at the same longitudinal positions $X/D = 4.76, 5.11, 5.30, 5.43$, and 5.50 . Figure 15 shows the pressure distribution at $X/D = 4.76$. As angle of attack is increased, variation of pressure with ϕ starts showing up. The agreement of the computed pressure with the data is good for $\alpha = 10.0^\circ$. Some discrepancy exists for the $\alpha = 4.0^\circ$ case. The computed result for this low angle of attack case has been checked and should be at least as accurate as the high angle of attack case at $X/D = 4.76$ (on the cylinder). The discrepancy at this particular location is not a result of computational inaccuracy. Possibly, the data at this location is suspect. Figure 16 through Figure 19 show the surface pressure distributions on the boattail at $X/D = 5.11, 5.30, 5.43$, and 5.50 , respectively. These figures again show the large variation of pressure with increase in angle of attack and with distance downstream on the boattail. The agreement of the computed pressures with the experimental data is not as good as it was found for the non-spinning case.

Figures 20 and 21 show the effect of spin on the pressure distribution at $X/D = 4.76$ for $\alpha = 4.0^\circ$ and $\alpha = 10.0^\circ$, respectively. As expected, the spin induces small changes in the pressure distribution. For the ten degree angle of attack case, the pressure is reduced slightly with spin. This is predicted by the computations and is also observed in the

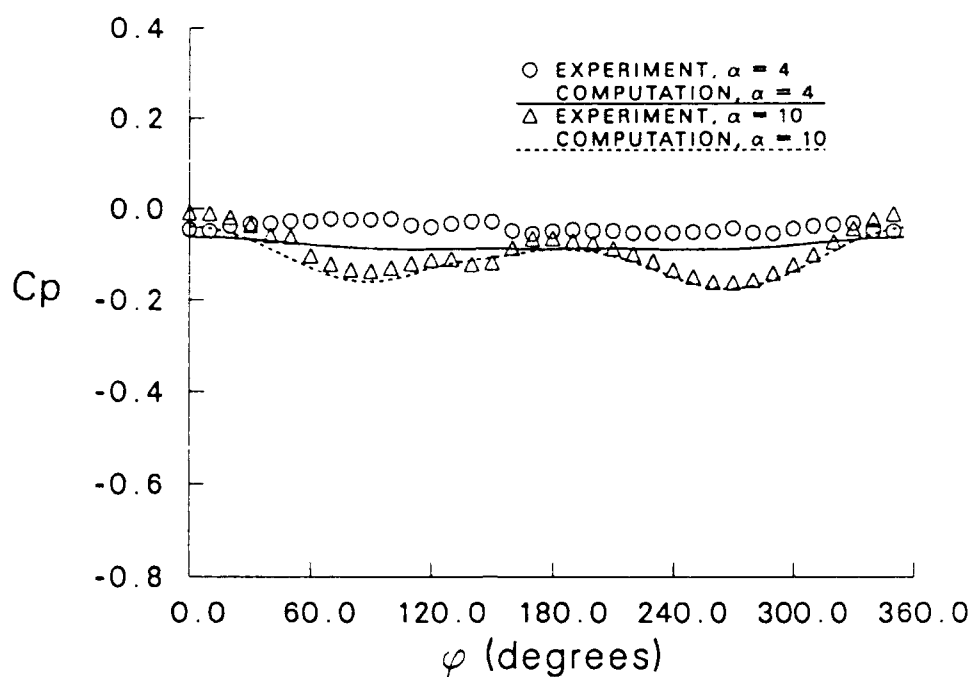


Figure 15. Circumferential surface pressure distribution, $P = 4900$ rpm, $M_\infty = 0.94$, $X/D = 4.76$.

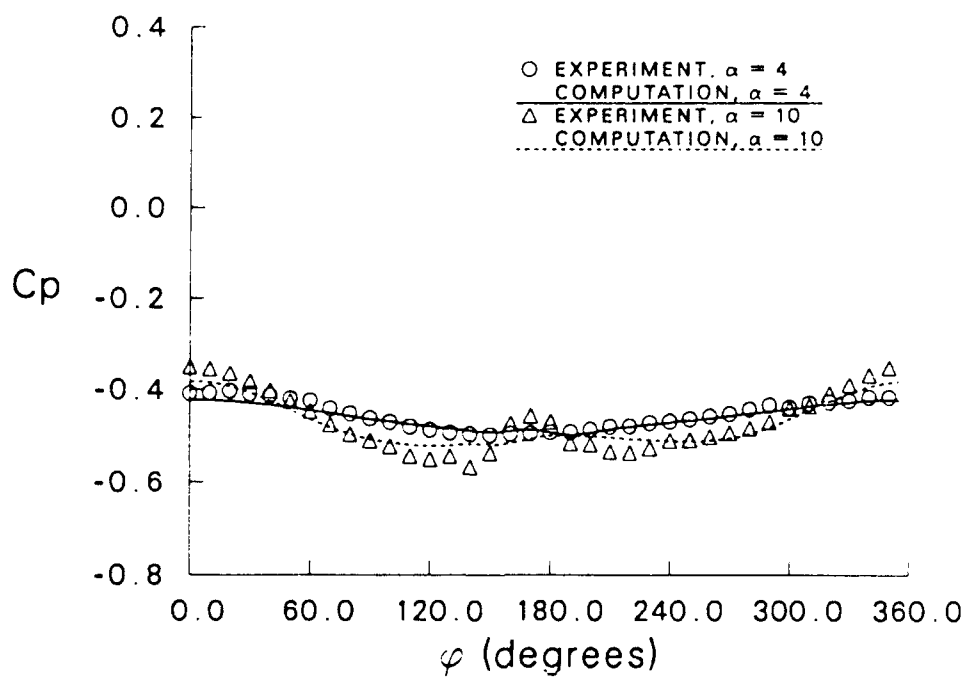


Figure 16. Circumferential surface pressure distribution, $P = 4900$ rpm, $M_\infty = 0.94$, $X/D = 5.11$.

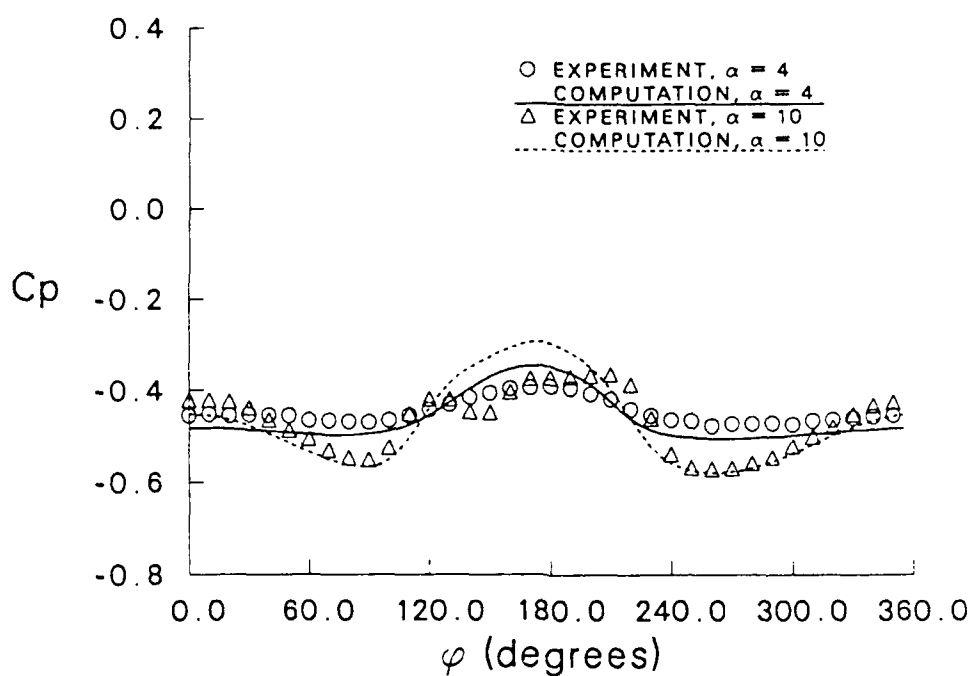


Figure 17. Circumferential surface pressure distribution, $P = 4900$ rpm, $M_{\infty}=0.94$, $X/D=5.30$.

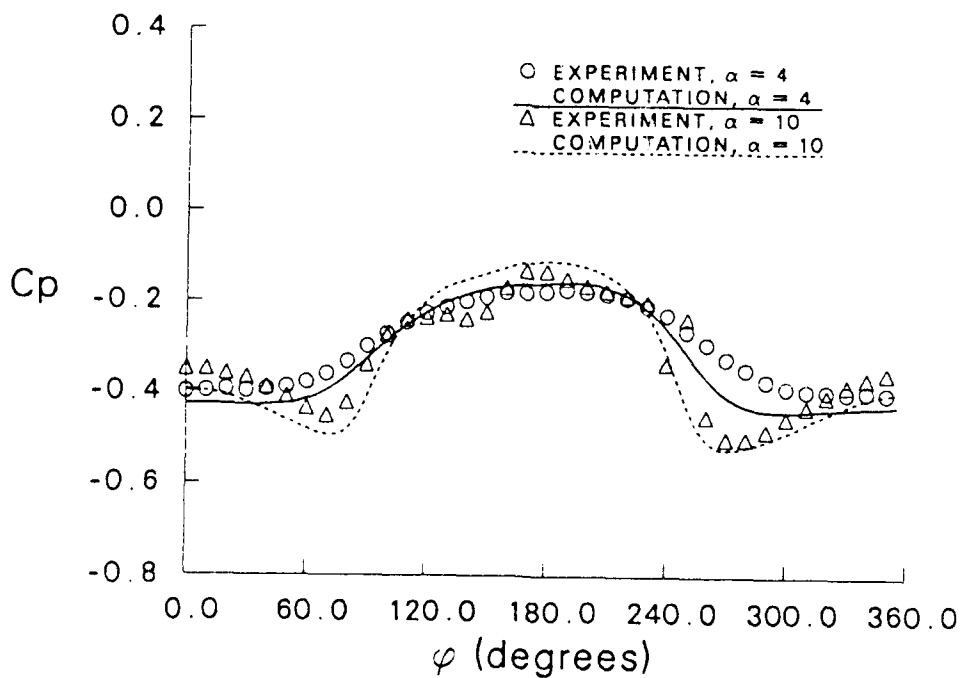


Figure 18. Circumferential surface pressure distribution, $P = 4900$ rpm, $M_{\infty}=0.94$, $X/D=5.43$.

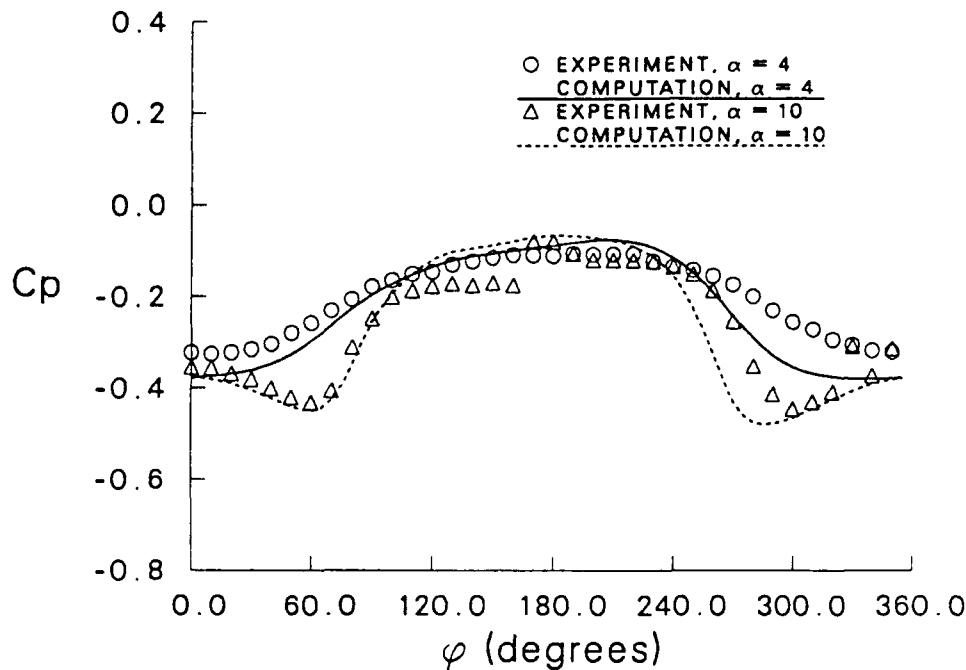


Figure 19. Circumferential surface pressure distribution, $P = 4900$ rpm, $M_\infty = 0.94$, $X/D = 5.50$.

experimental data (Miller and Molnar 1986). For the four degree angle of attack case, the computation again shows the same trend; however, the data show the reverse trend from $\phi = 40.0^\circ$ to $\phi = 160.0^\circ$. Figures 22 and 23 show the effect of spin on the pressure distribution at $X/D = 5.43$ for $\alpha = 4.0^\circ$ and $\alpha = 10.0^\circ$, respectively. For the zero spin cases shown here, the pressure distribution is symmetric about $\phi = 180.0^\circ$. As shown in Figure 22 for $\alpha = 4.0^\circ$, the agreement of computed pressure with data for the spinning case is good except for $\phi = 240.0^\circ$ to $\phi = 360.0^\circ$. As shown in Figure 23 for the $\alpha = 10.0^\circ$ case, the trend of computed pressure with spin seems to agree fairly well with the data; however, discrepancies do exist in the quantitative agreement. For this high angle of attack case, the experimental pressure distribution also shows a second pressure increase from $\phi = 140.0^\circ$ to $\phi = 170.0^\circ$ near the lee-side which is not predicted in the computed pressures.

The entire flowfield over the projectile including the base region is computed. Therefore, the computed results include any upstream influence the base region flow may have on the boattail flowfield. Surface pressures including the base pressure and the viscous stresses are known from the computed flow field and can be integrated to give the aerodynamic forces and moments.

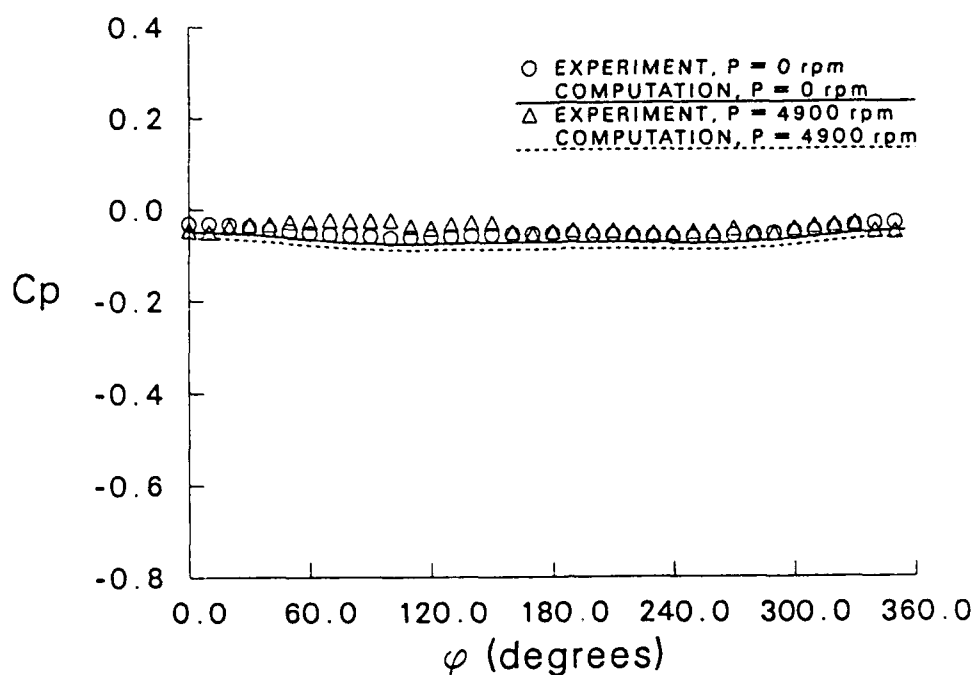


Figure 20. Circumferential surface pressure distribution, $M_\infty = 0.94$, $\alpha = 4.0^\circ$, $X/D = 4.76$.

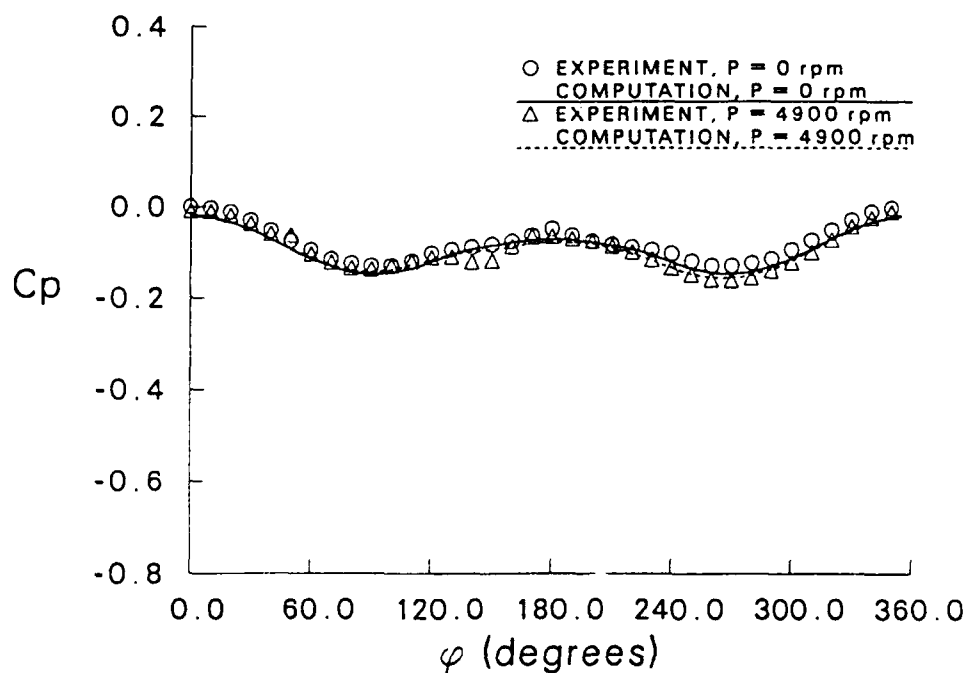


Figure 21. Circumferential surface pressure distribution, $M_\infty = 0.94$, $\alpha = 10.0^\circ$, $X/D = 4.76$.

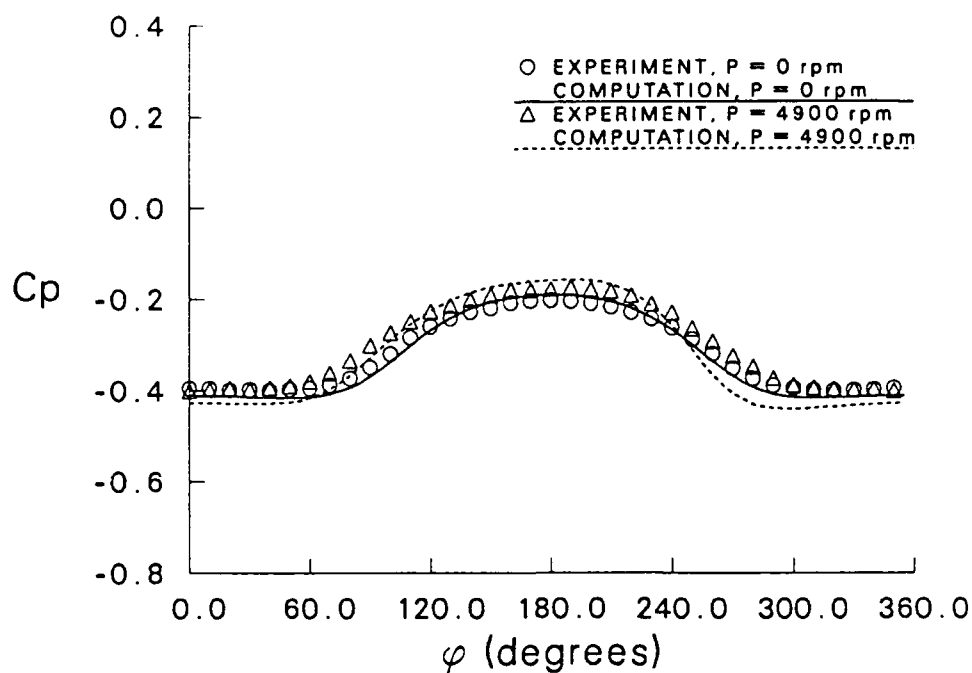


Figure 22. Circumferential surface pressure distribution, $M_\infty=0.94$, $\alpha = 4.0^\circ$, $X/D=5.43$.

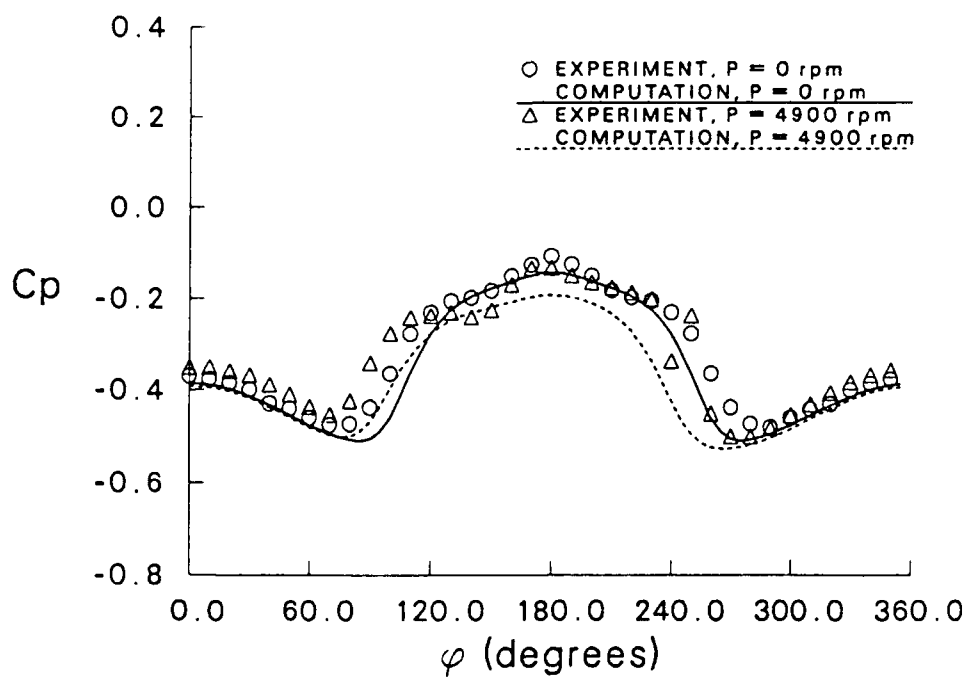


Figure 23. Circumferential surface pressure distribution, $M_\infty=0.94$, $\alpha = 10.0^\circ$, $X/D=5.43$.

Figure 24 and Figure 25 show the effect of angle of attack on normal force and pitching moment coefficient, respectively. Computed results are compared with the experimental data (Miller and Molnar 1986). In addition, these figures include Platou data (1973) which were obtained using a force and moment balance. As seen in both the computed and experimental data, the effect of spin on these coefficients is small. The normal force increases and the pitching moment coefficient decreases with angle of attack. This is the correct trend seen in both the computed results and data. As shown in Figure 24 for normal force coefficient, discrepancy of the order of 10 – 15% does exist between the computed result and experimentally obtained coefficient data at $\alpha = 4.0$. The agreement is much better at $\alpha = 10.0$. The discrepancy, particularly for the non-spinning cases at low angle of attack, is difficult to explain since the computed surface pressures are in good agreement with the experimentally measured pressures (Miller and Molnar 1986). Note that these experimental measurements were obtained at limited positions along the body (practically no points on the ogive and only five points on the boattail). As seen in Figure 25, the pitching moment coefficients obtained experimentally from measured surface pressures (Miller and Molnar 1986) are smaller than Platou data (1973). The computed results lie in between the two sets of experimental results.

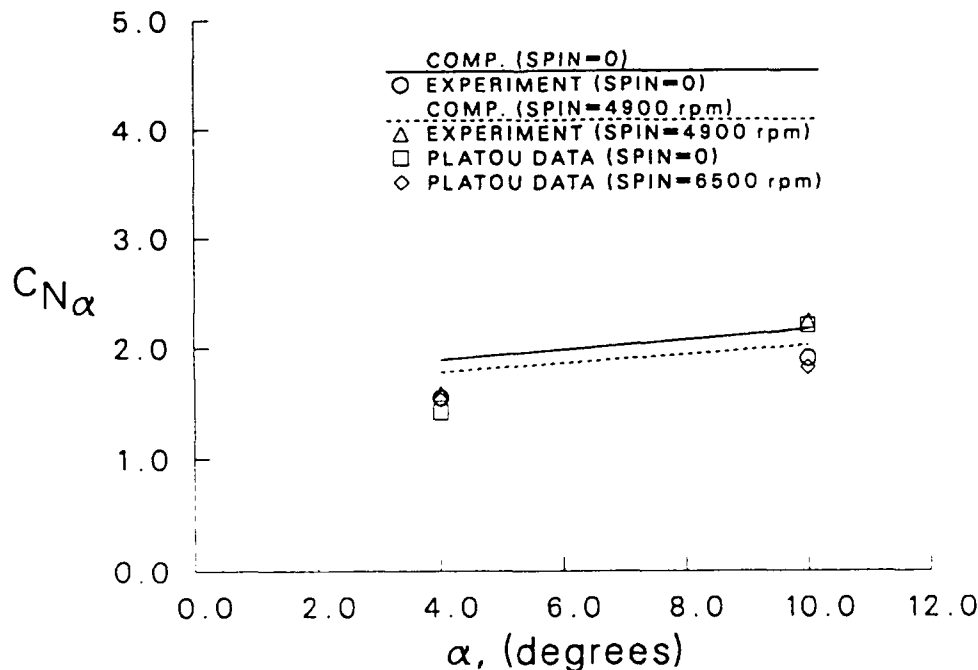


Figure 24. Normal force coefficient vs. angle of attack, $M_\infty=0.94$.

An aerodynamic coefficient which is of primary concern is the Magnus force coefficient, C_Y . Figure 26 shows the Magnus (side) force as it develops along the projectile for the spinning case at $\alpha = 4.0$ and 10.0° . For both of these cases, the side force contribution

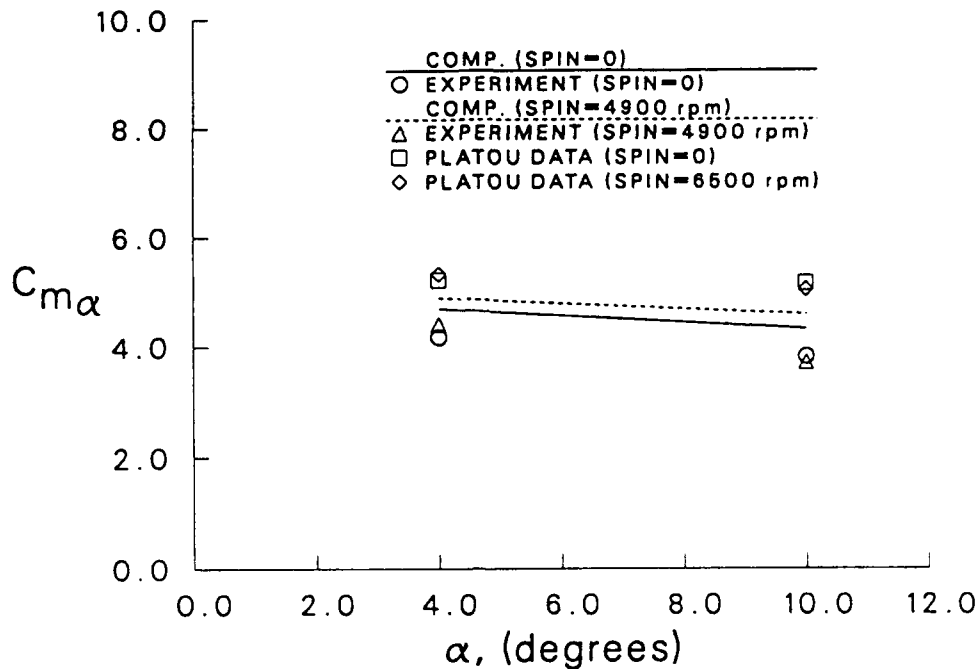


Figure 25. Pitching moment coefficient vs. angle of attack, $M_\infty=0.94$.

due to viscous stresses is negligible. The computed Magnus force shown in this figure then comes primarily from the integration of surface pressures. The computed results are shown in solid and dash lines. The open symbols represent the experimental results obtained from measured surface pressures (Miller and Molnar 1986). The closed symbols represent wind tunnel measurements (Platou and Nielsen 1973) where Magnus force and moment were obtained using a balance. For the $\alpha = 4.0^\circ$ case, both the computed result as well as the data show negligible contribution from the ogive section of the projectile and are in good agreement with each other. The side force drops right after the ogive-cylinder junction and then begins to level out. Again both results show this and the agreement is good until $X/D = 4.0$, half way through the cylindrical section. From here on the computed result shows a gradual drop in side force for the rest of the cylindrical section while the experimental result shows a sharp decline. At the boattail junction, there is a small increase in this force. This is followed by a sharp drop for almost all of the boattail except near the base corner where it increases somewhat. This trend can also be observed in the computed result and was shown in the earlier computations (Nietubicz, Sturek, and Heavey 1983). The final value of the side force agrees well with the experimental results at $\alpha = 4.0^\circ$. For the $\alpha = 10.0^\circ$ case, the trend of the side force distribution observed in the experimental result (Miller and Molnar 1986) can also be seen in the computed result. However, there is discrepancy between both of the experimental results as well as between the computation and experiment.

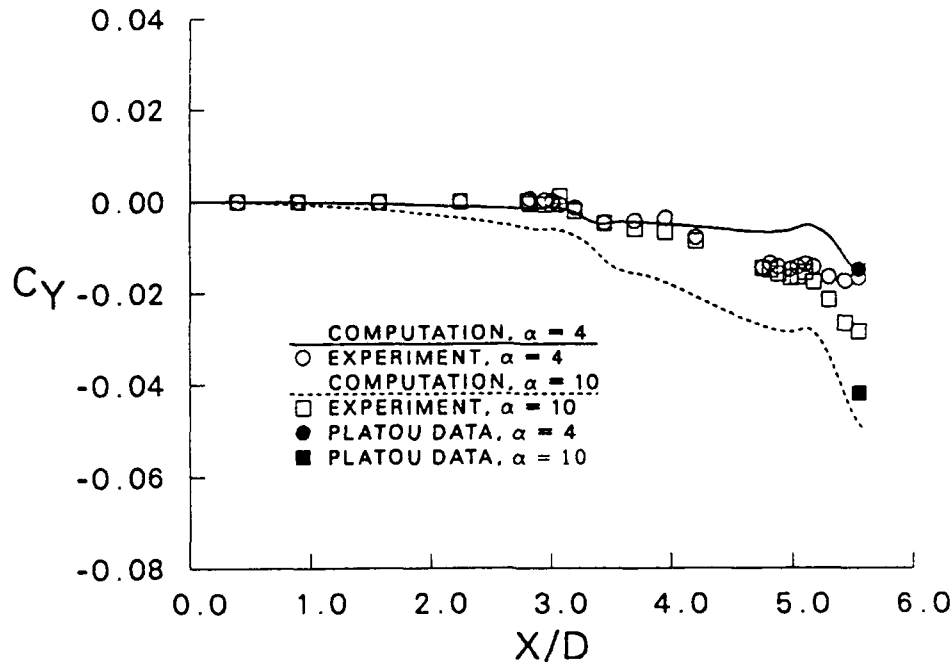


Figure 26. Development of Magnus force along the projectile, $M_{\infty}=0.94$.

Another aerodynamic coefficient which is very important from dynamic stability point of view is the Magnus (Yawing) moment coefficient, C_n . Figure 27 shows the Magnus moment coefficient for the projectile as a function of angle of attack. This moment coefficient is referenced to the center of gravity of the projectile which is located at 3.506 calibers from the nose. The computed result is shown by the solid line. The circles represent the experimental results (Miller and Molnar 1986) and the boxes represent Platou data (1973) obtained using a force and moment balance. In general, the computed result is in good agreement with the experimental data of Miller and Molnar (1986). For the $\alpha = 4.0^\circ$ case, both the computed result as well as the data are in reasonable agreement with each other. However, at $\alpha = 10.0$ there is some discrepancy or disagreement even between the two experimental results.

If the dependence of the Magnus moment is cubic in yaw level or angle of attack, the nonlinear variation of the moment coefficient is of the general form:

$$C_{n\alpha} = C_{n\alpha_0} + C_2\delta^2 \quad (7)$$

where $C_{n\alpha_0}$ is the zero-yaw value of Magnus moment coefficient, C_2 is the associated cubic coefficient and $\delta = \sin\alpha$. This analysis of the nonlinear Magnus moment yields the following result.

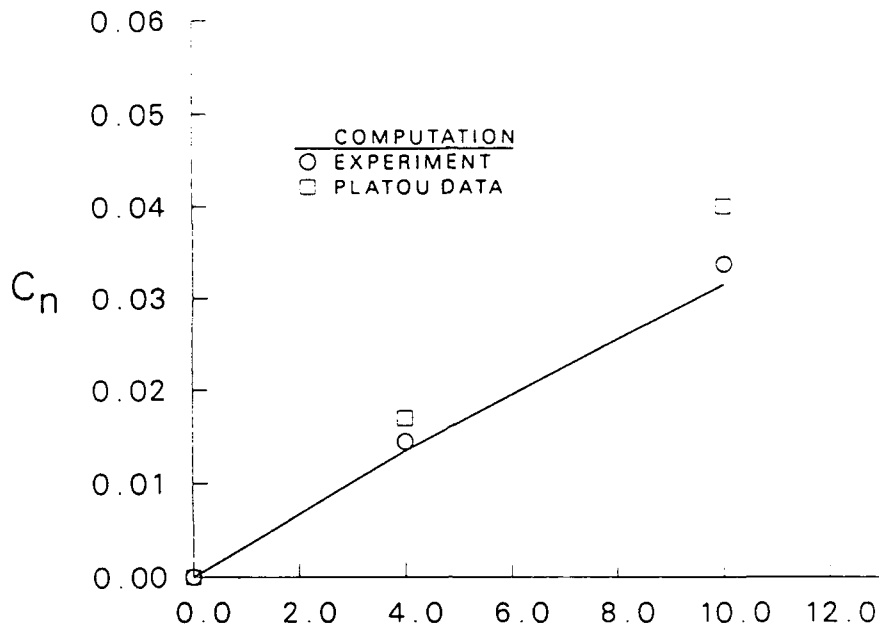


Figure 27. Magnus moment coefficient, $M_\infty=0.94$.

Table 1. Analysis of Nonlinear Magnus moment

Coefficient	Computation	Miller's experiment	Platou's data
$C_{n_{\alpha_0}}$.196	.210	.245
C_2	-.48	-.55	-.53

As shown in Table 1, the computed zero-yaw Magnus moment, $C_{n_{\alpha_0}}$, agrees to within about 6% and the computed cubic coefficient agrees to within about 12% of Miller's (1986) experimental data for the exact same shape and flow conditions. It should be noted that this result represents the first numerical prediction of a nonlinear Magnus moment at a transonic velocity.

As discussed earlier for this high angle of attack ($\alpha = 10.0^\circ$), the experimental pressure distribution shows a second pressure increase (hump) from $\phi = 140.0^\circ$ to $\phi = 170.0^\circ$ near the lee-side which is not predicted in the computed pressures (see Figure 22). It is well known that cross flow separation occurs on the projectile at high angles of attack. One way to possibly improve the numerical predictions for a high angle of attack case is to compute the lee-side vortical flow structure accurately. The turbulence level predicted by Baldwin-

Lomax algebraic turbulence model can be large in this vortical flow region. Limiting the outer turbulence length scale in the model in this region has led to improved numerical results (Schiff, Degani, and Cummings 1989) for supersonic and subsonic flows. This idea has been used here and a solution has been obtained for $\alpha = 10.0^\circ$. Figure 28 and Figure 29 show the circumferential surface pressure distribution at two longitudinal positions, one on the cylinder ($X/D = 4.76$) and the other on the boattail ($X/D = 5.50$). These figures show the result obtained by the modified turbulence model. This result is compared with that obtained by the original turbulence model as well as the experimental data. As shown in Figure 28 for $X/D = 4.76$, the result obtained with the modified turbulence model agrees better with the data and also contains the pressure hump near the lee-side. At $X/D = 5.50$ (see Figure 29) the agreement of the computed result with the data is not as good. However, the same trend of the variation of pressure with ϕ observed in the experimental data (Miller and Molnar 1986) has been clearly predicted in the computation with the modified turbulence model. This includes all the pressure variations near the lee-side. The aerodynamic forces and moments (including the Magnus force) obtained from these pressures were found to change very little from the results obtained with the original turbulence model.

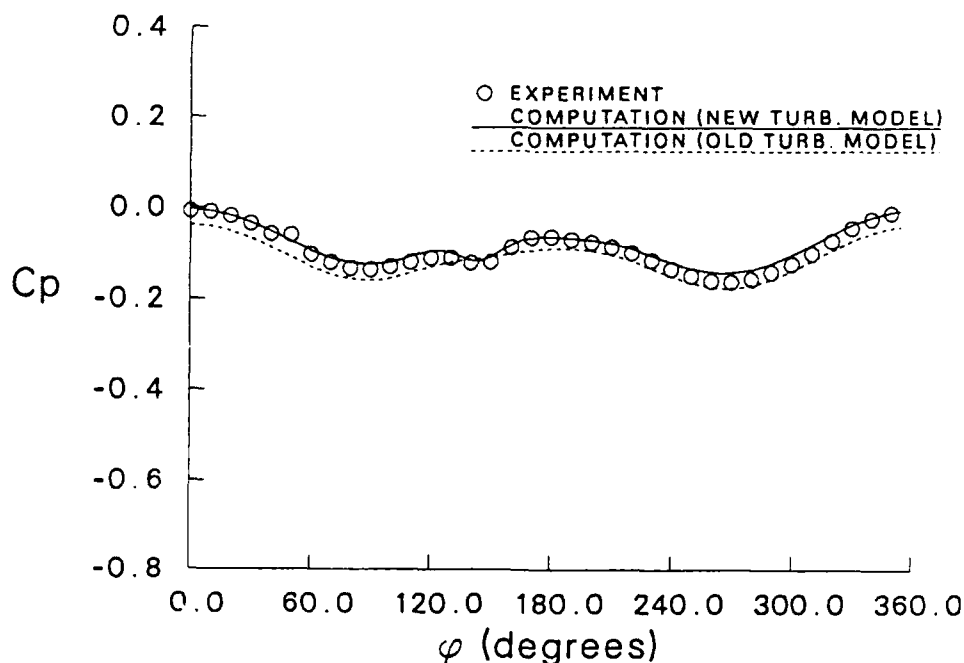


Figure 28. Circumferential surface pressure distribution, $M_\infty=0.94$, $\alpha = 10.0^\circ$, $X/D=4.76$.

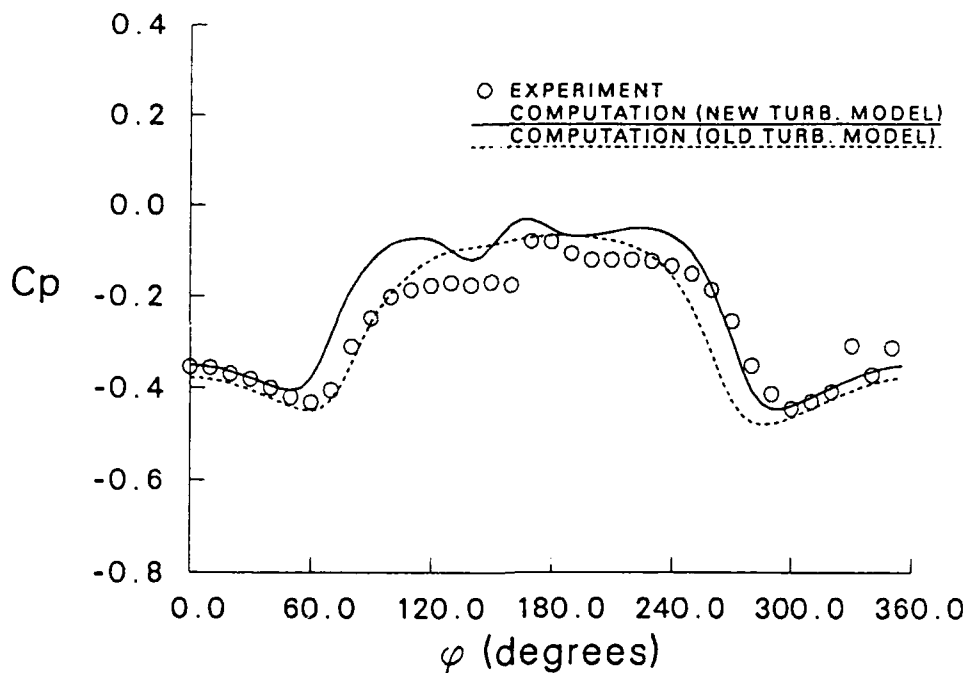


Figure 29. Circumferential surface pressure distribution, $M_\infty=0.94$, $\alpha = 10.0^\circ$, $X/D=5.50$.

6. CONCLUDING REMARKS

A zonal, implicit, time-marching Navier-Stokes computational technique has been used to compute three dimensional transonic flowfields over a secant-ogive-cylinder-boattail projectile. Flowfield computations have been performed at $M = 0.94$ for spin rates of 0 and 4900 rpm and at angles of attack, $\alpha = 0, 4$, and 10° .

Numerical results show the details of the flowfield such as Mach number contours and surface pressure distributions. Computed surface pressures are compared with available experimental data for the same conditions and the same configuration. Computed results show the large circumferential pressure variations over the boattail region as well as the non-linear effect of the angle of attack. Aerodynamic force and moment coefficients (normal force, pitching moment coefficient, Magnus force and Magnus moment) have been obtained from the computed pressures and have been compared with the data. Reasonable agreement has been obtained for the $\alpha = 4^\circ$ case for all these coefficients. The comparison is less satisfactory at $\alpha = 10^\circ$ particularly for the Magnus force. A modified turbulence model was used for this case which improved the pressure comparison somewhat. However, it did not change the force and moment results significantly. It should also be noted that for the high angle of attack case both experimental results do not agree with each other.

Analysis of non-linear Magnus moment was made to obtain both the zero-yaw Magnus moment as well as the cubic coefficient. The computed zero-yaw Magnus moment agrees to within about 6% and the computed cubic coefficient agrees to within about 12% of Miller's (1986) experimental data for the exact same shape and flow conditions. It should be noted that this result represents the first numerical prediction of nonlinear Magnus moment at a transonic velocity.

The accuracy in the experimentally obtained forces and moments for the spinning case is largely unknown. Also, it is not clear from the experiments whether the boundary layer was fully turbulent or if transition occurred on the projectile. The boundary layer was assumed to be turbulent in the computations. The agreement or disagreement of the computed forces and moments with the experimental results must be viewed in that light. The side force is very small and it is very difficult to obtain experimentally or computationally. The type of agreement achieved between the computation and experiments, particularly at low angle of attack is very encouraging. Additional code validation is required to better determine the accuracy of the predicted side force and moment by comparison with free flight results. This would involve full 3D computations at a low angle of attack for atmospheric flight conditions. Future efforts will then include running calculations at various transonic Mach numbers to determine the critical aerodynamic behavior in Magnus force and moment.

7. REFERENCES

- Nietubicz, C.J., Sturek, W.B. and Heavey, K.R. "Computations of Projectile Magnus Effect at Transonic Velocities," ARBRL-TR-02515, U.S. Army Ballistic Research Laboratory, Aberdeen Proving Ground, Maryland, August 1983. (AD A133212)
- Sahu, J. "Three Dimensional Base Flow Calculation for a Projectile at Transonic Velocity," BRL-MR-3610, U.S. Army Ballistic research Laboratory, Aberdeen Proving Ground, Maryland, June 1987. (AD A184171)
- Sahu, J. and Steger, J.L. "Numerical Simulation of Three Dimensional Transonic Flows," AIAA Paper No. 87-2293, Atmospheric Flight Mechanics Conference, Monterey, California, August 1987, (also see BRL-TR-2903, March 1988, (AD A194687)).
- Sahu, J. "Numerical Computations of Transonic Critical Aerodynamic Behavior," AIAA Journal, Vol. 28, No. 5, May 1990, pp. 807-816., (also see BRL-TR-2962, December 1988, (AD A202412)).
- Sahu, J. and Nietubicz, C.J. "Three Dimensional Flow Calculation for a Projectile with Standard and Dome Bases," BRL-TR-3150, U.S. Army Ballistic research Laboratory, Aberdeen Proving Ground, Maryland, September 1990. (AD A217282)
- Pulliam, T.H. and Steger, J.L. "On Implicit Finite-Difference Simulations of Three-Dimensional Flow," AIAA Journal, Vol. 18, No. 2, February 1982, pp. 159-167.
- Baldwin B.S. and Lomax, H. "Thin Layer Approximation and Algebraic Model for Separated Turbulent Flows," AIAA Paper No. 78-257, January 1978.
- Miller, M.C. and Molnar, J.W. "Wind Tunnel Measurements of the Magnus Induced Surface Pressures on a Spinning Artillery Projectile Model in the Transonic Speed Regime," CRDEC-TR-86081, Chemical Research, Development and Engineering Center, Aberdeen Proving Ground, Maryland, September 1986.
- Nietubicz, C.J., Heavey, K.R. and Steger, J.L. "Grid Generation Technique for Projectile Configurations," ARO Report 82-3, Proceedings of the 1982 Army Numerical Analysis and Computers Conference, August 1982.
- Platou, A.S. and Nielsen, G.I.T. "Some Aerodynamic Characteristics of the Artillery Projectile XM549," BRL-MR-2284, U.S. Army Ballistic Research Laboratory, Aberdeen Proving Ground, Maryland, April 1973.
- Schiff, L.B., Degani, D. and Cummings, R.M. "Numerical Simulation of Separated and Vortical Flows on Bodies at Large Angles of Attack," Proceedings of the Fourth Symposium on Numerical and Physical Aspects of Aerodynamic Flows, California State University, Long Beach, January 16-19, 1989.

INTENTIONALLY LEFT BLANK.

LIST OF SYMBOLS

a	speed of sound
c_p	specific heat at constant pressure
C_p	pressure coefficient
C_Y	Magnus or side force coefficient
C_N	normal force coefficient
C_m	pitching moment coefficient
D	projectile diameter
e	total energy per unit volume
$\hat{F}, \hat{G}, \hat{H}$	flux vectors in transformed coordinates
J	jacobian
M	Mach number
P	spin
Pr	Prandtl number
Pr_t	turbulent Prandtl number
\hat{q}	vector of dependent variables
R	body radius
\hat{S}	vector containing viscous terms
t	time
T	temperature
u, v, w	axial, circumferential, and normal velocity components of the Navier-Stokes equations
U, V, W	Contravariant velocities of the transformed Navier-Stokes equations
x, y, z	physical Cartesian coordinates

Greek Symbols

α	Angle of attack
γ	ratio of specific heats
κ	molecular and turbulent thermal conductivity
μ	molecular and turbulent viscosity
ξ, η, ζ	transformed coordinates
ρ	density
ϕ	circumferential angle

Subscripts

∞	free stream conditions
0	total

INTENTIONALLY LEFT BLANK.

<u>No. of Copies</u>	<u>Organization</u>	<u>No. of Copies</u>	<u>Organization</u>
2	Administrator Defense Technical Info Center ATTN: DTIC-DDA Cameron Station Alexandria, VA 22304-6145	1	Commander U.S. Army Missile Command ATTN: AMSMI-RD-CS-R (DOC) Redstone Arsenal, AL 35898-5010
1	Commander U.S. Army Materiel Command ATTN: AMCDRA-ST 5001 Eisenhower Avenue Alexandria, VA 22333-0001	1	Commander U.S. Army Tank-Automotive Command ATTN: ASQNC-TAC-DIT (Technical Information Center) Warren, MI 48397-5000
1	Commander U.S. Army Laboratory Command ATTN: AMSLC-DL 2800 Powder Mill Road Adelphi, MD 20783-1145	1	Director U.S. Army TRADOC Analysis Command ATTN: ATRC-WSR White Sands Missile Range, NM 88002-5502
2	Commander U.S. Army Armament Research, Development, and Engineering Center ATTN: SMCAR-IMI-I Picatinny Arsenal, NJ 07806-5000	1	Commandant U.S. Army Field Artillery School ATTN: ATSF-CSI Ft. Sill, OK 73503-5000
2	Commander U.S. Army Armament Research, Development, and Engineering Center ATTN: SMCAR-TDC Picatinny Arsenal, NJ 07806-5000	(Class. only) 1	Commandant U.S. Army Infantry School ATTN: ATSH-CD (Security Mgr.) Fort Benning, GA 31905-5660
1	Director Benet Weapons Laboratory U.S. Army Armament Research, Development, and Engineering Center ATTN: SMCAR-CCB-TL Watervliet, NY 12189-4050	(Unclass. only) 1	Commandant U.S. Army Infantry School ATTN: ATSH-CD-CSO-OR Fort Benning, GA 31905-5660
(Unclass. only) 1	Commander U.S. Army Armament, Munitions and Chemical Command ATTN: AMSMC-IMF-L Rock Island, IL 61299-5000	1	Air Force Armament Laboratory ATTN: WL/MNOI Eglin AFB, FL 32542-5000 <u>Aberdeen Proving Ground</u>
1	Director U.S. Army Aviation Research and Technology Activity ATTN: SAVRT-R (Library) M/S 219-3 Ames Research Center Moffett Field, CA 94035-1000	2	Dir, USAMSAA ATTN: AMXSY-D AMXSY-MP, H. Cohen
		1	Cdr, USATECOM ATTN: AMSTE-TC
		3	Cdr, CRDEC, AMCCOM ATTN: SMCCR-RSP-A SMCCR-MU SMCCR-MSI
		1	Dir, VLAMO ATTN: AMSLC-VL-D
		10	Dir, BRL ATTN: SLCBR-DD-T

No. of
Copies Organization

- 6 Commander
U.S. Army Armament Research,
Development, and Engineering Center
ATTN: SMCAR-AET-A,
R. Kline
R. Collett
R. Botticelli
H. Hudgins
J. Grau
S. Kahn
Picatinny Arsenal, NJ 07806-5000
- 1 Department of the Army
Office of the Product Manager
155-mm Howitzer, M109A6, Paladin
ATTN: SFAE-AR-HIP-IP, Mr. R. De Kleine
Picatinny Arsenal, NJ 07806-5000
- 1 Commander
U.S. Naval Surface Warfare Center
ATTN: Dr. F. Moore
Dahlgren, VA 22448
- 3 Commander
Naval Surface Warfare Center
ATTN: Code R44,
Dr. F. Priolo
Dr. A. Wardlaw
K24, B402-12, Dr. W. Yanta
White Oak Laboratory
Silver Spring, MD 20903-5000
- 2 USAF Wright Aeronautical Laboratories
ATTN: AFWAL/FIMG,
Dr. J. Shang
Mr. N. E. Scaggs
Wright-Patterson AFB, OH 45433-6553
- 3 Air Force Armament Laboratory
ATTN: AFATL/FXA,
Stephen C. Korn
Bruce Simpson
Dave Belk
Eglin AFB, FL 32542-5434

No. of
Copies Organization

- 2 DARPA
ATTN: Dr. Peter Kemmey
Dr. James Richardson
1400 Wilson Blvd.
Arlington, VA 22209
- 1 Director
Los Alamos National Laboratory
ATTN: Mr. Bill Hogan, MS G770
Los Alamos, NM 87545
- 3 Director
Sandia National Laboratories
ATTN: Dr. W. Oberkampff
Dr. F. Blottner
Dr. W. Wolfe
Division 1636
Albuquerque, NM 87185
- 4 Director
National Aeronautics and Space Administration
Langley Research Center
ATTN: Tech Library
Mr. D. M. Bushnell
Dr. M. J. Hemsch
Dr. J. South
Langley Station
Hampton, VA 23665
- 6 Director
National Aeronautics and Space Administration
Ames Research Center
ATTN: MS-227-8, L. Schiff
MS-258-1,
T. Holst
D. Chaussee
M. Rai
P. Kutler
W. VanDalsem
Moffett Field, CA 94035
- 1 United States Military Academy
Department of Mechanics
ATTN: LTC Andrew L. Dull
West Point, NY 10996

<u>No. of Copies</u>	<u>Organization</u>
3	University of California, Davis Department of Mechanical Engineering ATTN: Prof. H. A. Dwyer Prof. J. Steger Dr. B. Meakin Davis, CA 95616
1	Massachusetts Institute of Technology ATTN: Tech Library 77 Massachusetts Ave. Cambridge, MA 02139
1	Virginia Polytechnic Institute and State University Department of Aerospace and Ocean Engineering ATTN: Dr. Clark H. Lewis Blacksburg, VA 24061
1	Pennsylvania State University Department of Aerospace Engineering ATTN: Dr. G. S. Dulikrovich University Park, PA 16802
1	University of Illinois at Urbana Champaign Department of Mechanical and Industrial Engineering Urbana, IL 61801
1	University of Maryland Department of Aerospace Engineering ATTN: Dr. J. D. Anderson, Jr. College Park, MD 20742
1	University of Notre Dame Department of Aeronautical and and Mechanical Engineering ATTN: Prof. T. J. Mueller Notre Dame, IN 46556
1	University of Texas Department of Aerospace Engineering and Engineering Mechanics ATTN: Dr. D. S. Dolling Austin, TX 78712-1055

<u>No. of Copies</u>	<u>Organization</u>
1	University of Delaware Department of Mechanical Engineering ATTN: Dr. John Meakin, Chairman Newark, DE 19716
1	University of Florida College of Engineering Department of Engineering Sciences ATTN: Prof. C. C. Hsu Gainesville, FL 32611
2	Interferometrics, Inc. ATTN: Rene Larriva Eric L. Strobel 8150 Leesburg Pike Vienna, VA 22180
3	Science and Technology, Inc. ATTN: Dr. Alan Glasser Mr. Bruce Lohman Dr. Dave Maurizi 1700 North Moore St., Suite 1920 Arlington, VA 22209
1	Grumann Aerospace Corporation Aerophysics Research Department ATTN: Dr. R. E. Melnik Bethpage, NY 11714
1	AEDC Calspan Field Service ATTN: MS 600, Dr. John Benek Tullahoma, TN 37389
1	Advanced Technology Center Arvin/Calspan Aerodynamics Research Department ATTN: Dr. M. S. Holden P.O. Box 400 Buffalo, NY 14225
	<u>Aberdeen Proving Ground</u>
5	Cdr, CRDEC, AMCCOM ATTN: SMCCR-RSP-A, M. Miller J. Molnar D. Wise D. Weber SMCCR-RSP, A. Stuempfle

INTENTIONALLY LEFT BLANK.

USER EVALUATION SHEET/CHANGE OF ADDRESS

This laboratory undertakes a continuing effort to improve the quality of the reports it publishes. Your comments/answers below will aid us in our efforts.

1. Does this report satisfy a need? (Comment on purpose, related project, or other area of interest for which the report will be used.) _____

2. How, specifically, is the report being used? (Information source, design data, procedure, source of ideas, etc.) _____

3. Has the information in this report led to any quantitative savings as far as man-hours or dollars saved, operating costs avoided, or efficiencies achieved, etc? If so, please elaborate. _____

4. General Comments. What do you think should be changed to improve future reports? (Indicate changes to organization, technical content, format, etc.) _____

BRL Report Number BRL-TR-3265 Division Symbol _____

Check here if desire to be removed from distribution list. _____

Check here for address change. _____

Current address: Organization _____
Address _____

DEPARTMENT OF THE ARMY

Director
U.S. Army Ballistic Research Laboratory
ATTN: SLCBR-DD-T
Aberdeen Proving Ground, MD 21005-5066

OFFICIAL BUSINESS

BUSINESS REPLY MAIL

FIRST CLASS PERMIT No 0001, APG, MD

Postage will be paid by addressee.

Director
U.S. Army Ballistic Research Laboratory
ATTN: SLCBR-DD-T
Aberdeen Proving Ground, MD 21005-5066

NO POSTAGE
NECESSARY
IF MAILED
IN THE
UNITED STATES